Programmable Heisenberg interactions between Floquet qubits

Long B. Nguyen,[1, 2, *] Yosep Kim,[1, 2, 3, †] Akel Hashim,[1, 2] Noah Goss,[1, 2] Brian Marinelli,[1, 2]
Bibek Bhandari,[4] Debmalya Das,[5, 4] Ravi K. Naik,[1, 2] John Mark Kreikebaum,[2, 6]
Andrew N. Jordan,[4, 5] David I. Santiago,[1, 2] and Irfan Siddiqi[1, 2, 6]

[1]*Computational Research Division, Lawrence Berkeley National Laboratory, Berkeley, California 94720, USA*
[2]*Department of Physics, University of California, Berkeley, California 94720, USA*
[3]*Center for Quantum Information, Korea Institute of Science and Technology (KIST), Seoul 02792, Korea*
[4]*Institute for Quantum Studies, Chapman University, Orange, CA 92866, USA*
[5]*Department of Physics and Astronomy, University of Rochester, Rochester, NY 14627, USA*
[6]*Materials Science Division, Lawrence Berkeley National Laboratory, Berkeley, California 94720, USA*

The fundamental trade-off between robustness and tunability is a central challenge in the pursuit of quantum simulation and fault-tolerant quantum computation. In particular, many emerging quantum architectures[1,2] are designed to achieve high coherence at the expense of having fixed spectra and consequently limited types of controllable interactions. Here, by adiabatically transforming fixed-frequency superconducting circuits into modifiable Floquet qubits, we demonstrate an XXZ Heisenberg interaction with fully adjustable anisotropy. This interaction model is on one hand the basis for many-body quantum simulation of spin systems[3], and on the other hand the primitive for an expressive quantum gate set[4]. To illustrate the robustness and versatility of our Floquet protocol, we tailor the Heisenberg Hamiltonian and implement two-qubit iSWAP, CZ, and SWAP gates with estimated fidelities of 99.32(3)%, 99.72(2)%, and 98.93(5)%, respectively. In addition, we implement a Heisenberg interaction between higher energy levels and employ it to construct a three-qubit CCZ gate with a fidelity of 96.18(5)%. Importantly, the protocol is applicable to various fixed-frequency high-coherence platforms, thereby unlocking a suite of essential interactions for high-performance quantum information processing. From a broader perspective, our work provides compelling avenues for future exploration of quantum electrodynamics and optimal control using the Floquet framework[5].

Introduction

The capability to coherently choreograph interactions between qubits is the foundation for the recent advances in quantum technologies. A quintessential example is the manipulation of the quantum Heisenberg model for the simulation of many-body quantum spin systems[3,6,7], which has led to the recent discoveries of intriguing physical phenomena such as discrete time crystal[8], phantom spin-helix states[9], and formation of photon bound states[10]. The Heisenberg interactions are also the primitives for expressive multi-qubit gates[4] which play important roles in quantum algorithms[11] and quantum error correction[12,13]. Therefore, endowing quantum architectures with such archetypal interactions significantly extends their capabilities and performance.

The required tunability in solid-state quantum devices generally entails additional decoherence channels, demanding design overhead, and increased operational complexity. For example, in the domain of superconducting circuits, the performance in flux-tunable devices is typically limited by unavoidable $1/f$ noise arising from the surrounding environment. Meanwhile, fixed-frequency platforms such as single-junction transmon[14,15] and fluxonium[16] biased at the half-integer flux quantum[17] have the best coherence times to date, but their native interactions are limited to the cross-resonance[18,19] and longitudinal couplings[20,21]. Introducing additional tunable couplers enables a parametric transverse coupling, but the performance is undermined by the couplers' coherence and spurious couplings[22].

In this work, we present a reliable and hardware-efficient protocol to synthesize Floquet qubits[23,24] from statically coupled single-junction transmon qubits using time-periodic microwave drives, showing that the adiabatic mapping procedure can be hastened by exploiting a shortcuts-to-adiabaticity (STA) technique[25–27]. Then, we implement an XXZ Heisenberg interaction between these Floquet qubits, described by the Hamiltonian

$$\hat{\mathcal{H}}_{\mathrm{XXZ}}/\hbar = \sum_{i,j} J_{\mathrm{XY}}(\hat{\sigma}_{\mathrm{x}}^i \hat{\sigma}_{\mathrm{x}}^j + \hat{\sigma}_{\mathrm{y}}^i \hat{\sigma}_{\mathrm{y}}^j) + J_{\mathrm{ZZ}}\hat{\sigma}_{\mathrm{z}}^i \hat{\sigma}_{\mathrm{z}}^j, \qquad (1)$$

and demonstrate that the transverse spin-exchange and longitudinal spin-spin interaction terms can be adjusted independently by tailoring the drive parameters.

To validate the robustness and practicality of the protocol, we characterize two-qubit iSWAP, CZ, and SWAP gates which correspond to different anisotropy $J_{\mathrm{ZZ}}/J_{\mathrm{XY}}$, achieving estimated fidelities of 99.32(3)%, 99.72(2)%, and 98.93(5)%, respectively. In addition, we show that the Floquet-engineered interactions can be broadly applied to other levels in the system. Specifically, we explore the swapping between the qutrit states $|11\rangle$ and $|02\rangle$, then employ it to implement a three-qubit CCZ gate which is locally equivalent to the Toffoli gate[28], achieving an estimated fidelity of 96.18(5)%. Our work exemplifies the operational principles of Floquet qubits and illustrates their broad potential, thus opening promising pathways for future developments of the Floquet framework in enhancing the capabilities of fixed-frequency solid-state quantum platforms.
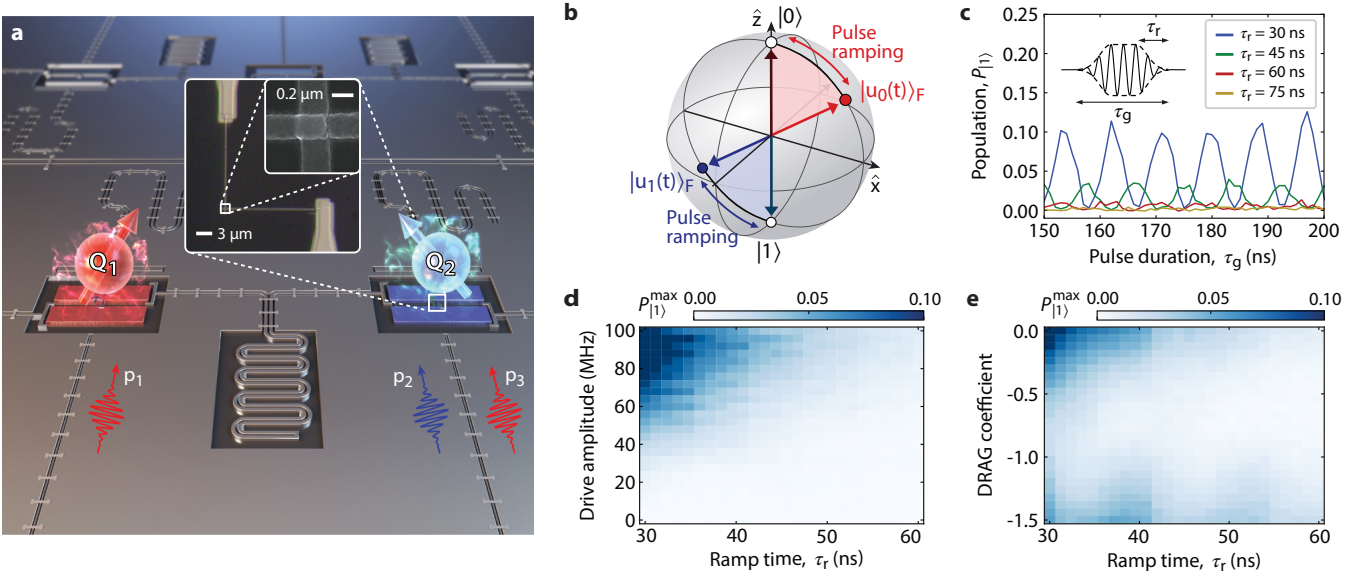
Fig. 1. Floquet qubit. a, Experimental schematic depicting two single-junction transmon qubits Q_1 (red) and Q_2 (blue) coupled via a shared coplanar-waveguide resonator resulting in an effective static coupling[29]. Microwave pulses are applied to the transmission lines situated below the capacitor pads to sculpt the Floquet qubits and control single-qubit rotations. The Heisenberg interactions are programmed by tailoring pulses p1, p2, and p3. **b,** Bloch sphere representation of the adiabatic transformation from a bare qubit in the lab frame to a Floquet qubit in the rotating frame. **c,** Population in the excited state $P_{|1\rangle}$ of Q_1 when subjected to a microwave pulse with amplitude 100 MHz, detuning -40 MHz, ramp time τ_r, and duration τ_g. Nonadiabaticity manifests as finite oscillations for short ramp time τ_r. **d,** Dependence of the maximum state leakage $P_{|1\rangle}^{\max}$ on the pulse's amplitude and ramp time τ_r. The drive is applied at the same frequency from **c**. **e,** Dependence of $P_{|1\rangle}^{\max}$ on the pulse's ramp time τ_r and DRAG coefficient. The drive amplitude and frequency are the same from **c**.

Synthesizing Floquet qubits

Figure 1**a** depicts the superconducting device used in the experiment. It consists of single-junction transmon qubits[14] which are pairwise coupled via mutual coplanar waveguide resonators[29,30]. Details of the quantum device and experimental setup are presented in Methods. Although the frequencies of the qubits are fixed after fabrication, Floquet engineering has recently emerged as a powerful tool that allows the sculpting of effective Hamiltonians that are otherwise unavailable[31], thus promising a new dimension to tune the system. Here, we synthesize Floquet qubits using detuned periodic microwave drives and tailor them to engineer the Hamiltonian given by Eq. (1).

The mapping is described by Floquet formalism as follows. The Hamiltonian of a two-level spin-half system subjected to a periodic driving field with amplitude A, frequency ω_d, and phase φ is given as

$$\hat{\mathcal{H}}_q(t)/\hbar = -\frac{\omega_q}{2}\hat{\sigma}_z + A\cos(\omega_d t + \varphi)\,\hat{\sigma}_x, \qquad (2)$$

where $\hbar\omega_q$ is the energy gap of the two-level system, and $\hat{\sigma}_z$ and $\hat{\sigma}_x$ represent the Pauli operators. There exists no static eigenenergies and eigenstates of the system as solutions of the time-dependent Schrödinger equation $i\hbar\partial_t|\psi(t)\rangle = \hat{\mathcal{H}}_q(t)|\psi(t)\rangle$. However, due to the periodicity of $\hat{\mathcal{H}}_q(t)$, the Schrödinger equation can be modified into the Floquet equation[5,32], $\left(\hat{\mathcal{H}}_q(t) - i\hbar\partial_t\right)|u_n(t)\rangle_F =$

$\hbar\varepsilon_n|u_n(t)\rangle_F$, and static quasienergies $\hbar\varepsilon_n$ can be found for time-periodic Floquet states $|u_n(t)\rangle_F = |u_n(t+2\pi/\omega_d)\rangle_F$. Here the Floquet states are denoted with subscript F to distinguish them from the bare states in the lab frame. The Floquet and bare states are interconvertible following the relation

$$|u_n(t)\rangle_F = e^{i\varepsilon_n t}|\psi_n(t)\rangle. \qquad (3)$$

Interestingly, $e^{ik\omega_d t}|u_n(t)\rangle_F$ with integer k also satisfies the Floquet equation and has quasienergy $\hbar(\varepsilon_n + k\omega_d)$, resulting in an infinite transition spectrum[32], $\varepsilon_1 - \varepsilon_0 = k\omega_d \pm \sqrt{A^2 + (\omega_d - \omega_q)^2}$, where the plus(minus) sign corresponds to red(blue) detuned drive. In addition, the drive phase φ acts as a time translation operator on the Hamiltonian in Eq. (2), $|u_n(t)\rangle_F \to |u_n(t + \varphi/\omega_d)\rangle_F$. These show how the Floquet states and their quasienergies depend on the drive parameters A, φ, and ω_d, which we can use to tailor the driven systems (See Methods for detailed Floquet formalism).

To prepare a Floquet qubit with the desired properties, we have to continuously map the undriven qubit to the Floquet basis, as shown in Fig. 1**b**. If the transformation is performed abruptly, there exists finite tunneling between the Floquet basis states, and the process becomes nonadiabatic. According to Adiabatic Theorem[32], the tunneling rate is proportional to dA/dt, that is, the target Floquet qubit corresponding to a larger drive amplitude must be transformed using a longer ramp time.
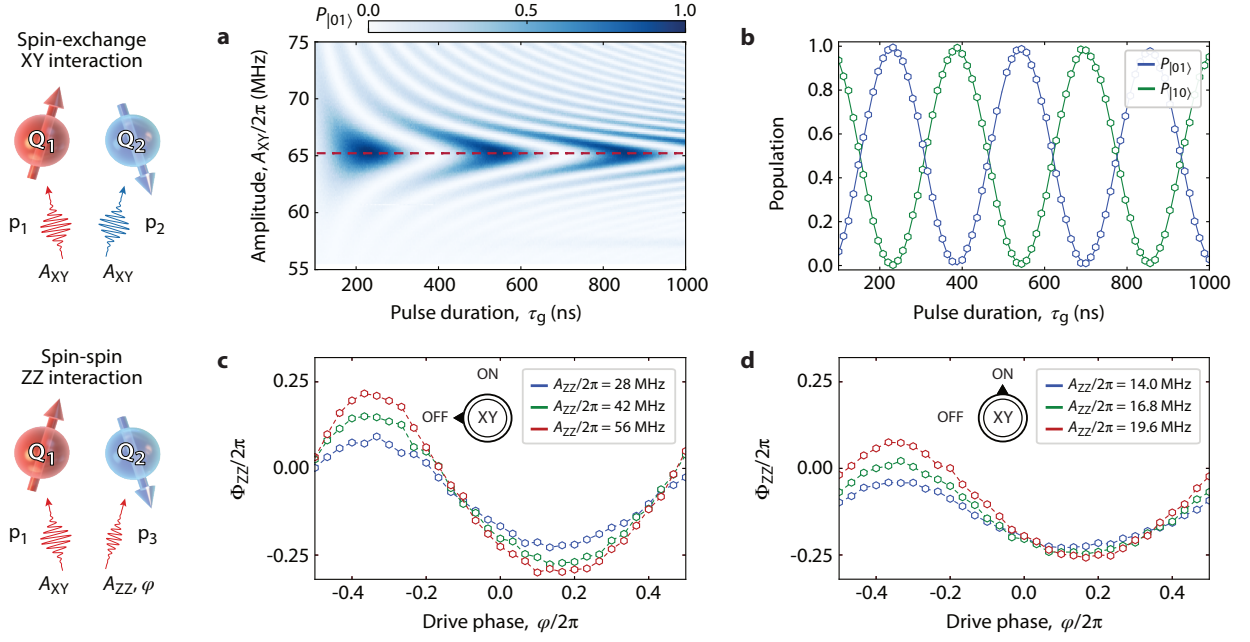
Fig. 2. **Floquet-engineered** XXZ **Heisenberg interaction**. **a,** Chevron pattern showing the dependence of $P_{|01\rangle}$ on the amplitude A_{XY} and duration τ_{g} of pulses p_1 and p_2 for qubits initialized in $|10\rangle$ (top left schematic). The pulses are applied at frequencies 40 MHz red(blue)-detuned from $Q_{1(2)}$'s $|0\rangle \leftrightarrow |1\rangle$ transition with DRAG coefficients $\lambda_{\mathrm{DRAG}} = -(+)0.6$ and ramp time $\tau_{\mathrm{r}} = 50$ ns. **b,** Coherent oscillation between $|10\rangle$ and $|01\rangle$ for the optimal pulse amplitude $A_{\mathrm{XY}}/2\pi = 65.2$ MHz highlighted by the red dashed line in **a**. **c,** Extracted longitudinal coupling angle Φ_{ZZ} between the qubits after p_1 and p_3 are applied at 40 MHz red-detuned from Q_1's transition frequency (bottom left schematic). They are 200-ns-long, with ramp time $\tau_r = 50$ ns and DRAG coefficient $\lambda_{\mathrm{DRAG}} = -0.6$. p_1's amplitude is fixed at $A_{\mathrm{XY}}/2\pi = 65.2$ MHz, while p_2's amplitude A_{ZZ} and phase φ are varied to tune the ZZ coupling rate. **d,** Extracted longitudinal coupling angle Φ_{ZZ} between the qubits after being subjected to all three pulses. The amplitude A_{XY} of p_1 and p_2 is tuned to induce a full $|10\rangle \leftrightarrow |01\rangle$ swap, while the amplitude A_{ZZ} and phase φ of p_3 are varied to tune the ZZ rate during the swap.

We experimentally explore this by irradiating qubit Q_1 with a cosine-ramp pulse with different pulse durations τ_{g} and ramp times τ_{r}, then measuring its excited state population $P_{|1\rangle}$. The drive amplitude is set to be 100 MHz in terms of on-resonant Rabi frequency, and the drive frequency is red-detuned from Q_1's transition frequency by 40 MHz. Nonadiabatic effects then manifest as finite excited state populations after the pulse, which oscillates with respect to the pulse duration due to the dynamical phase accumulation of the Floquet qubit (Fig. 1**c**). Evidently, shorter ramp times correspond to more severe nonadiabatic effects. In addition, the result in Fig. 1**d** confirms that a larger drive amplitude requires a longer ramp time to satisfy the adiabatic condition.

Interestingly, we find that using an STA technique known as derivative removal by adiabatic gate (DRAG)[26,27] helps reduce nonadiabatic effects substantially. As shown in Fig. 1**e**, the excited state leakage corresponding to a short-ramp pulse can be suppressed by adding a quadrature component to the pulse with amplitude $A_{\mathrm{Q}} = \lambda_{\mathrm{DRAG}} \times dA(t)/dt$. Case in point, τ_{r} can be reduced from 60 ns to 30 ns by employing a DRAG coefficient $\lambda_{\mathrm{DRAG}} = -0.7$. This suggests that advanced optimal control techniques can be explored to further accelerate the mapping procedure.

Tailoring Heisenberg interactions

Having established the general conditions for adiabatic mapping between undriven qubit states and Floquet states, we next orchestrate the microwave pulses to engineer the XXZ Heisenberg interaction in Eq. (1) between the Floquet qubits. The interaction Hamiltonian describing the coupling between Q_1 and Q_2 in Fig. 1**a** is $\hat{\mathcal{H}}_{\mathrm{int}}/\hbar = J\hat{\sigma}_{\mathrm{x}}^{(1)}\hat{\sigma}_{\mathrm{x}}^{(2)}$, where J is the static coupling strength, the superscripts are qubit indices, and the Pauli operators are defined in the undriven basis. This interaction can be described by a Floquet Hamiltonian using the relation given by Eq. (3),

$$\hat{\mathcal{H}}_{\mathrm{int,F}}/\hbar = J \sum_{a,b,c,d} c_{ab}^{(1)}(t)c_{cd}^{(2)}(t)e^{i(\varepsilon_{ab}^{(1)}+\varepsilon_{cd}^{(2)})t}\hat{f}_{ab}^{(1)}(t)\hat{f}_{cd}^{(2)}(t),$$

(4)

where $\varepsilon_{ab}^{(k)} \equiv \varepsilon_b^{(k)} - \varepsilon_a^{(k)}$, $c_{ab}^{(k)}(t) = \langle\psi_a^{(k)}(t)|\hat{\sigma}_{\mathrm{x}}^{(k)}|\psi_b^{(k)}(t)\rangle$, $\hat{f}_{ab}^{(k)}(t) = |u_a^{(k)}(t)\rangle_{\mathrm{F}}\langle u_b^{(k)}(t)|_{\mathrm{F}}$ for qubit Q_k, and $a, b, c, d \in \{0, 1\}$ for two qubits. The fast oscillation dynamics can be neglected by invoking the rotating wave approximation, leaving only the terms that follow energy conservation law, $\varepsilon_{ab}^{(1)} + \varepsilon_{cd}^{(2)} = 0$ for $abcd \in \{0110, 1001, 0000, 0011, 1100, 1111\}$. Inspecting the reduced Hamiltonian then gives us insight on the types of interactions present between the qubits.

On one hand, the terms satisfying $\varepsilon_{01}^{(1)} = \varepsilon_{01}^{(2)}$ correspond to the transverse XY spin-exchange interaction in Eq. (1) with $J_{\mathrm{XY}} = J\langle c_{01}^{(1)} c_{10}^{(2)}\rangle_t = J\langle c_{10}^{(1)} c_{01}^{(2)}\rangle_t$, where $\langle...\rangle_t$ denotes the time-average value. This process follows the conventional wisdom that an XY exchange-type interaction between two coupled spins occurs when they are brought into resonance with each other. On the other hand, the rest of the reduced Hamiltonian produces the longitudinal ZZ spin-spin coupling in Eq. (1), $J_{\mathrm{ZZ}} = J\langle c_{11}^{(1)} c_{11}^{(2)} + c_{00}^{(1)} c_{00}^{(2)} - c_{00}^{(1)} c_{11}^{(2)} - c_{11}^{(1)} c_{00}^{(2)}\rangle_t$. Consequently, we can program the transverse and longitudinal interactions independently by tailoring the quasienergies with periodic microwave drives.

We proceed to validate this principle as follows. First, we engineer a pure transverse XY spin-exchange interaction corresponding to an XX Heisenberg model where the anisotropy is zero, $\Delta = J_{\mathrm{ZZ}}/J_{\mathrm{XY}} = 0$. Given that Q_1's frequency is lower than that of Q_2, their quasienergy differences $\varepsilon_{01}^{(k)}$ can be brought into resonance if $Q_1(Q_2)$ is driven with red(blue) detuned microwaves (Extended Data Fig. 3b). After preparing the qubits in $|10\rangle$, we apply two such pulses (p_1 and p_2 in Fig. 1a and top left panel of Fig. 2) with the same duration τ_{g} and amplitude A_{XY} at a detuning frequency of 40 MHz. We observe a coherent population transfer to state $|01\rangle$ that forms a chevron pattern as a function of τ_{g} and A_{XY}, signifying a transverse coupling between the qubits (Fig. 2a). Notably, although the interaction occurs between the Floquet qubits in the dressed frame, the adiabatic connection ascertains the exchange between the bare qubit states after the reverse mapping, which bears resemblance to the latching mechanism in classical electronics. Indeed, at the optimal drive amplitude $A_{\mathrm{XY}}/2\pi = 65.2$ MHz (Fig. 2b), $|10\rangle$ and $|01\rangle$ exhibit coherent oscillations at a rate of 3.2 MHz, which is limited by the static coupling constant J (Methods). The lack of fast oscillatory behavior is a clear indication of the high mapping fidelity.

Next, we proceed to induce a pure longitudinal ZZ spin-spin coupling corresponding to an Ising interaction between the Floquet qubits. This can be accomplished by irradiating microwave drives p_1 on Q_1 and p_3 on Q_2 (Fig. 1a and bottom left panel of Fig. 2) at a frequency 40 MHz red-detuned from Q_1. p_1's amplitude is fixed at $A_{\mathrm{XY}}/2\pi = 65.2$ MHz, while p_3 has parameterized amplitude A_{ZZ} and phase φ. For weak driving, $A_{\mathrm{XY,ZZ}} \ll \omega_{\mathrm{q,d}}$, the ZZ rate is given as $J_{\mathrm{ZZ}} \approx 2JA_{\mathrm{XY}} A_{\mathrm{ZZ}} \cos(\varphi)/\sqrt{(A_{\mathrm{XY}}^2 + \delta_1^2)(A_{\mathrm{ZZ}}^2 + \delta_2^2)}$, where δ_k is the detuning from Q_k's frequency (Methods). Importantly, while the transverse coupling rate J_{XY} shown above is essentially limited by the static coupling strength J, the longitudinal coupling rate J_{ZZ} can be tuned by two knobs, namely the drives' amplitudes and phase difference. We characterize the interaction by first initializing the two qubits in the superposition state $(|0\rangle + |1\rangle) \otimes (|0\rangle + |1\rangle)/2$, applying the pulses as specified, and then extracting the entangling phase $\Phi_{\mathrm{ZZ}}(\tau_{\mathrm{g}}) = \int_0^{\tau_{\mathrm{g}}} J_{\mathrm{ZZ}}\, t\, dt$ using tomographic reconstruction assisted by numerical optimization (Methods). As shown in Fig. 2c, this phase depends on p_3's amplitude A_{ZZ} and phase φ, consistent with our description.

Leveraging the independent controls of the transverse and longitudinal interactions, we now tailor the interplay between them to adjust the anisotropy of the XXZ Heisenberg interaction model. To this end, we apply p_1 and p_2 pulses with their amplitude A_{XY} and duration τ_{g} tuned to induce a full $|10\rangle \leftrightarrow |01\rangle$ swap (Fig. 2b). Pulse p_3 is then jointly applied, albeit with parameterized amplitude A_{ZZ} and phase φ. Incorporating the swap condition into the tomography analysis, we extract the longitudinal entangling phase Φ_{ZZ} which depends on p_3's parameters as shown in Fig. 2d. This demonstrates that the anisotropy of the model given by Eq. (1) can be programmed in a versatile fashion.

Benchmarking Heisenberg interactions

The programmable Heisenberg interaction endows quantum processors with an extensive quantum gate set as well as the capability to simulate many-body spin-half systems. Here we benchmark our Floquet-engineered Heisenberg interactions by characterizing a suite of representative two-qubit gates: the iSWAP, CZ, and SWAP gates resulting from the XX Heisenberg model, Ising model, and XXX Heisenberg model, respectively. Accordingly, an iSWAP unitary arises naturally from a pure transverse XY interaction with the pulse duration τ_{g} corresponding to a full swap in Fig. 2b, implemented by applying p_1 and p_2. In practice, there is a dynamical ZZ coupling originating from microwave crosstalk, which can be tracked and compensated by simultaneously applying p_3 with appropriate amplitude and phase. Likewise, a CZ gate is realized when p_1 and p_3 are calibrated to bring up an entangling phase $\Phi_{\mathrm{ZZ}}/2\pi = 0.25$. Finally, we tailor all three pulses to sculpt an isotropic XXX Heisenberg interaction that leads to a SWAP gate at the correct gate time τ_{g}, at which both iSWAP and CZ conditions are satisfied. Our calibration steps are detailed in Methods.

To quantify the gates' performances without state preparation and measurement (SPAM) errors, we employ cycle benchmarking (CB)[33], which tailors all errors into stochastic Pauli channels via Pauli twirling and results in tight bounds on the estimated fidelity (Methods). In addition to the dressed cycles that include the implemented gates, we also measure the reference cycle and extract its errors to estimate the relevant gate fidelities. Figure 3a shows the Pauli fidelity distribution histograms of both the reference and dressed cycles corresponding to the intended two-qubit gates. Comparing the dressed cycle data to the reference cycle result allows us to estimate the average gate fidelities of the implemented iSWAP, CZ, and SWAP gates to be 99.32(3)%, 99.72(2)%, and 98.93(5)%, respectively. We note that these gates are expandable to a continuous fSim gate set[4,34], which can be integrated into arbitrary quantum circuits compatible with fixed-frequency qubits by using more advanced circuit compilation tools[35] or efficient physical Z-gates.
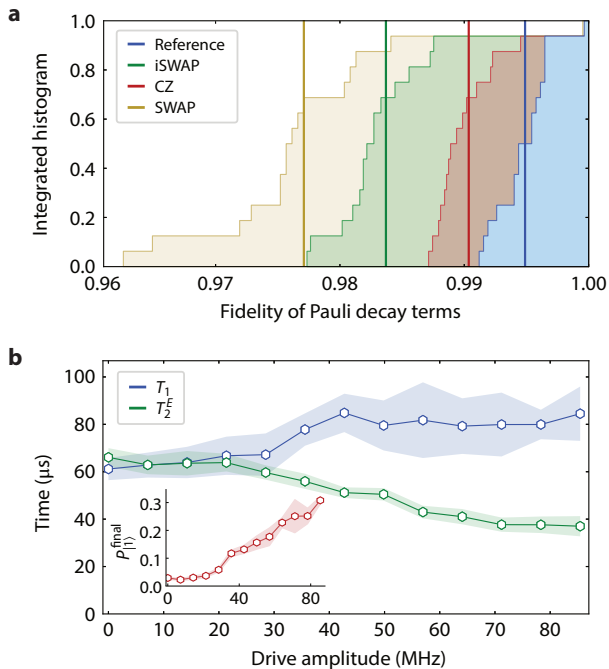
Fig. 3. **Characterization of two-qubit gates**. **a.** Cycle benchmarking results showing the Pauli fidelity histogram for the Reference, iSWAP, CZ, and SWAP cycles, with the solid vertical lines indicating the average values. The corresponding average two-qubit gate fidelities are estimated to be 99.32(3)%, 99.72(2)%, and 98.93(5)%, respectively. **b.** Effective coherence time statistics of the Floquet qubit created by adiabatically driving Q_1 at a red-detuning of 40 MHz. These are acquired by sampling 20 different sweeps for each curve. Inset: Excited state population at the end of the 355-μs-long $|0\rangle \rightarrow |1\rangle$ measurement sequence.

Our analysis attributes the limitations of these results primarily to decoherence mechanisms (Methods). Intriguingly, the Floquet qubits appear to exhibit coherence times deviating from those of the bare qubits, as shown in Fig. 3**b**. The measurements are performed using nominal energy relaxation and echo dephasing procedures on the bare Q_1, however, with the addition of a microwave pulse applied 40 MHz red-detuned from its $|0\rangle \leftrightarrow |1\rangle$ transition during idle periods. The results are post-selected to yield the populations of the desired states, and the experiment is repeated over twenty iterations to eliminate any potential outlier. While the dynamics remain the same at small drive amplitudes, T_1 tends to increase while T_2^E tends to decrease at strong driving before nonadiabaticity sets in. Interestingly, we also discover a heating mechanism that enlarges the excited state population in the bare qubit at the end of the 355-μs-long $|0\rangle \rightarrow |1\rangle$ measurement sequence, with $P_{|1\rangle}^{\text{final}}$ increases with the driving amplitude (Fig. 3**b**, inset). We include additional details in Methods, and hope that future investigations can find efficient approaches to mitigate these effects, reminiscent of the recent progress in driven ultracold atom systems[36].

Floquet qutrit and three-qubit gate

So far, the fundamental and universal importance of spin physics motivates our discussion to portray the implemented Floquet qubits as ideal spin-half's. Nevertheless, many solid-state systems, including the transmon, naturally include multiple relevant energy levels. Making use of them expands the Hilbert space, allowing more information to be encoded, which leads to hardware-efficient execution of quantum algorithms[37,38] and hastens the development of fault-tolerant computation[39,40]. We now show that the presented protocol can be tailored for multi-level systems, thereby paving new pathways for quantum information processing using Floquet qudits.

Specifically, we leverage the techniques described so far to induce a transverse qutrit-qutrit interaction between the states $|11\rangle$ and $|02\rangle$. Although the cross-Kerr coupling has been explored[41], such an energy-exchange interaction is still absent in fixed-frequency qutrits. While this is a useful ternary gate itself, we presently show that integrating it in a sequence involving multiple qubits allows the implementation of a three-body controlled-controlled-Z gate (CCZ)[28], which plays an important role in quantum applications such as factorization[42,43] and quantum error correction[44,45]. To this end, we add to the experiment Q_3, which is coupled to the right side of Q_2 in Fig. 1**a**, and use Q_2 and Q_3 as control qubits (subscripted c), while Q_1 is designated as the target (subscripted t).

Figure 4**a** depicts the energy diagram of Q_2 and Q_3. Our approach to engineer the interaction primarily involves applying a microwave pulse to Q_3 at a frequency red-detuned from its $|1\rangle \leftrightarrow |2\rangle$ transition to create a Floquet qutrit such that the control Floquet states $|11\rangle_c$ and $|02\rangle_c$ become degenerate. After initializing the control qubits in $|11\rangle_c$, we apply such a pulse with ramp time $\tau_r = 170$ ns, DRAG coefficient $\lambda_{\text{DRAG}} = -0.6$, and varying amplitude A_{XY} and duration τ_g, which are tailored to ensure adiabaticity at a red-detuning of 22 MHz. The transverse interaction between $|11\rangle_c$ and $|02\rangle_c$ then manifests into an asymmetric chevron pattern with respect to A_{XY} and τ_g in Fig. 4**b**. Interestingly, we observe that the optimal swap condition occurs at a stronger amplitude relative to the symmetric point.

A CCZ unitary can be implemented using the sequence given in Fig. 4**c**. The final CPhase gate on the control qubits are tuned to bring the effective operation on them to be $\hat{I} \otimes \hat{I}$ at the end of the sequence. After calibrating the individual gates, we verify the entanglement between the three qubits by extracting the Z-phase of the target qubit (Q_1) for different control states, and observe a phase shift of approximately π for $|10\rangle_c$ (Fig. 4**d**), which evinces the CCZ effect. The sequence can be further sandwiched between single-qubit rotations on Q_1 to construct a Toffoli gate. The process can be straightforwardly validated by measuring the truth table, from which we extracted a fidelity of 92.9(1)% (Fig. 4**e**). Finally, we employ CB to benchmark the CCZ gate (Fig. 4**f**), achieving a fidelity of 96.18(5)%, with the main error resulting from decoherence (Methods).
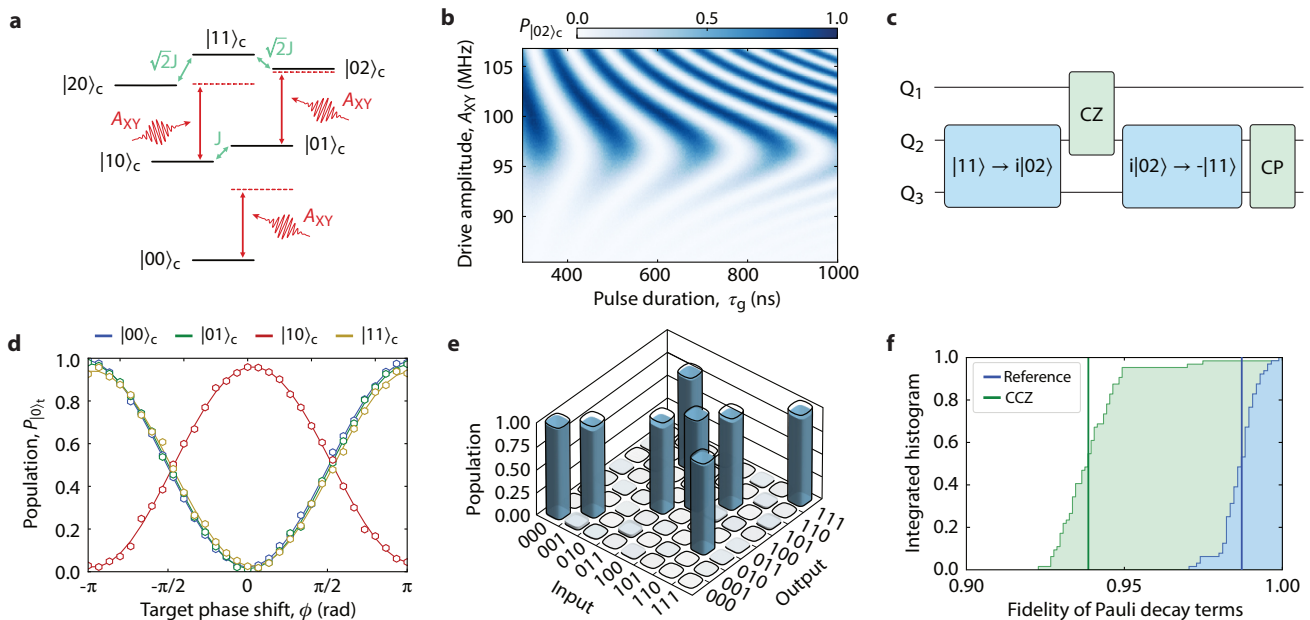
Fig. 4. **Floquet qutrit and three-qubit CCZ gate**. **a,** Energy diagram of two coupled transmon circuits Q_2 and Q_3, with the subscript c denoting they are control qubits. A microwave drive with amplitude A_{XY} is applied at a frequency red-detuned from Q_3's $|1\rangle \leftrightarrow |2\rangle$ transition to create a Floquet qutrit. **b,** Chevron pattern showing a coherent flip-flop between Q_2 and Q_3's states $|11\rangle_c$ and $|02\rangle_c$, which depends on the amplitude A_{XY} and duration τ_g of the pulse. The red-detuning is 22 MHz, the ramp time is $\tau_r = 170$ ns, and the DRAG coefficient is $\lambda_{DRAG} = -0.6$. **c,** Gate sequence used to implement a three-qubit CCZ unitary, with Q_1 as the target qubit and Q_2, Q_3 as the control qubit pair. **d,** A conditionality measurement, using a Ramsey-like sequence $\{R_Y^{(t)}(\frac{\pi}{2}), \text{CCZ}, R_Z^{(t)}(\phi), R_Y^{(t)}(\frac{\pi}{2})\}$, reveals the dependence of Q_1's phase on the states of Q_2 and Q_3 under the CCZ gate implemented using the sequence in **c**, which is characteristic of a three-body entanglement. **e,** Truth table of the implemented Toffoli gate with a corresponding fidelity of 92.9(1)%. **f,** Cycle benchmarking result showing the Pauli fidelity distributions of the three-qubit reference cycle and CCZ dressed cycle, with the solid vertical lines indicating the average values. The average gate fidelity is estimated to be 96.18(5)%.

Outlook

Our work embodies a transformative application of Floquet engineering in superconducting circuits where periodic drives are used to map static qubits to Floquet qubits with modifiable quasienergies, granting access to an unconventional tuning channel. We demonstrate the practicality and versatility of this approach by synthesizing Floquet qubits and qutrits, then realizing an XXZ Heisenberg interaction between them with fully tunable anisotropy. The robustness of the scheme is reflected from the high gate fidelities, while the current limitations are straightforward to overcome. On one hand, the coherence times of the fixed-frequency transmon qubits in the experiment are relatively low, therefore we expect better performance in state-of-the-art devices. On the other hand, the coupling rate is primarily limited by the static coupling constant J, which can be increased substantially in future devices. In addition, the pulse shape used in this work is quite simple, so we believe that advanced STA techniques can be employed to engineer shorter gates, further reducing errors from dephasing in the future. We note that the full potential of this framework lies upon its adaptation to other synthetic fixed-frequency quantum architectures with better projected performance such as fluxonium quantum processor[46].

Having illustrated the useful properties of Floquet qubits and set the stage for immediate improvements, we envision the following avenues to propel the concept in complementary directions. The protocol presented here involves transforming back to the static qubit so normal operations such as readout and single-qubit gates can be employed without recalibration. In the future, a Floquet qubit can be permanently defined by applying a continuous periodic drive in principle, streamlining the process and unlocking new opportunities for novel control and readout methods[24]. This approach also allows *in-situ* tuning of the qubit frequencies, thus provides a practical solution for problems arising from two-level-system defects and spectral crowding. In another route, the ramp time can be reduced substantially if we operate in the diabatic regime, where the mapping is close to ideal despite finite transition between the Floquet states. We expect the potential development of optimal control within the Floquet framework to provide a reliable approach in this regime. Last but not least, the heating effect which correlates with the reduction in T_2 reminisces a similar effect in cold atom systems which has been successfully suppressed[36]. This calls for deeper understanding of the quantum thermodynamics in driven solid-state systems and possible mitigation strategies in the future.

ACKNOWLEDGMENTS

* nbaolong89@gmail.com; Equal contribution.
† yosep9201@gmail.com; Equal contribution.

[1] A. Gyenis, A. Di Paolo, J. Koch, A. Blais, A. A. Houck, and D. I. Schuster, PRX Quantum **2**, 030101 (2021).

[2] I. Siddiqi, Nat. Rev. Mater. **6**, 875 (2021).

[3] L. Savary and L. Balents, Rep. Prog. Phys. **80**, 016502 (2016).

[4] I. D. Kivlichan, J. McClean, N. Wiebe, C. Gidney, A. Aspuru-Guzik, G. K.-L. Chan, and R. Babbush, Phys. Rev. Lett. **120**, 110501 (2018).

[5] J. H. Shirley, Phys. Rev. **138**, B979 (1965).

[6] H. Bernien et al., Nature **551**, 579 (2017).

[7] P. N. Jepsen, J. Amato-Grill, I. Dimitrova, W. W. Ho, E. Demler, and W. Ketterle, Nature **588**, 403 (2020).

[8] J. Zhang et al., Nature **543**, 217 (2017).

[9] P. N. Jepsen, Y. K. Lee, H. Lin, I. Dimitrova, Y. Margalit, W. W. Ho, and W. Ketterle, Nat. Phys. **18**, 899 (2022).

[10] A. Morvan et al., Preprint at https://arxiv.org/abs/2206.05254 (2022).

[11] K. Bharti et al., Rev. Mod. Phys. **94**, 015004 (2022).

[12] A. G. Fowler, M. Mariantoni, J. M. Martinis, and A. N. Cleland, Phys. Rev. A **86**, 032324 (2012).

[13] J. Ghosh and A. G. Fowler, Phys. Rev. A **91**, 020302 (2015).

[14] J. Koch et al., Phys. Rev. A **76**, 042319 (2007).

[15] H. Paik et al., Phys. Rev. Lett. **107**, 240501 (2011).

[16] V. E. Manucharyan, J. Koch, L. I. Glazman, and M. H. Devoret, Science **326**, 113 (2009).

[17] L. B. Nguyen, Y.-H. Lin, A. Somoroff, R. Mencia, N. Grabon, and V. E. Manucharyan, Phys. Rev. X **9**, 041041 (2019).

[18] J. M. Chow et al., Phys. Rev. Lett. **107**, 080502 (2011).

[19] Y. Kim et al., Nat. Phys. **18**, 783 (2022).

[20] B. K. Mitchell et al., Phys. Rev. Lett. **127**, 200502 (2021).

[21] K. X. Wei et al., Phys. Rev. Lett. **129**, 060501 (2022).

[22] M. Ganzhorn et al., Phys. Rev. Research **2**, 033447 (2020).

[23] Z. Huang, P. S. Mundada, A. Gyenis, D. I. Schuster, A. A. Houck, and J. Koch, Phys. Rev. Applied **15**, 034065 (2021).

[24] A. Gandon, C. Le Calonnec, R. Shillito, A. Petrescu, and A. Blais, Phys. Rev. Applied **17**, 064006 (2022).

[25] D. Guéry-Odelin, A. Ruschhaupt, A. Kiely, E. Torrontegui, S. Martínez-Garaot, and J. G. Muga, Rev. Mod. Phys. **91**, 045001 (2019).

[26] F. Motzoi, J. M. Gambetta, P. Rebentrost, and F. K. Wilhelm, Phys. Rev. Lett. **103**, 110501 (2009).

[27] J. M. Gambetta, F. Motzoi, S. T. Merkel, and F. K. Wilhelm, Phys. Rev. A **83**, 012308 (2011).

[28] A. Fedorov, L. Steffen, M. Baur, M. P. da Silva, and A. Wallraff, Nature **481**, 170 (2011).

[29] J. Majer et al., Nature **449**, 443 (2007).

[30] A. Blais, A. L. Grimsmo, S. M. Girvin, and A. Wallraff, Rev. Mod. Phys. **93**, 025005 (2021).

[31] C. Weitenberg and J. Simonet, Nat. Phys. **17**, 1342 (2021).

[32] C. Deng, F. Shen, S. Ashhab, and A. Lupascu, Phys. Rev. A **94**, 032323 (2016).

[33] A. Erhard et al., Nat. Commun. **10**, 1 (2019).

[34] B. Foxen et al., Phys. Rev. Lett. **125**, 120504 (2020).

[35] J. Chen, D. Ding, C. Huang, and Q. Ye, Preprint at https://arxiv.org/abs/2105.02398 (2021).

[36] K. Viebahn, J. Minguzzi, K. Sandholzer, A.-S. Walter, M. Sajnani, F. Görg, and T. Esslinger, Phys. Rev. X **11**, 011057 (2021).

[37] A. Bocharov, M. Roetteler, and K. M. Svore, Phys. Rev. A **96**, 012306 (2017).

[38] P. Gokhale, J. M. Baker, C. Duckering, N. C. Brown, K. R. Brown, and F. T. Chong, in Proceedings of the 46th International Symposium on Computer Architecture (ACM, 2019) p. 554.

[39] E. T. Campbell, Phys. Rev. Lett. **113**, 230501 (2014).

[40] S. Muralidharan, C.-L. Zou, L. Li, J. Wen, and L. Jiang, New J. Phys. **19**, 013026 (2017).

[41] N. Goss et al., Preprint at https://arxiv.org/abs/2206.07216 (2022).

[42] P. W. Shor, SIAM J. Comput. **26**, 1484 (1997).

[43] C. Gidney and M. Ekerå, Quantum **5**, 433 (2021).

[44] T. J. Yoder, R. Takagi, and I. L. Chuang, Phys. Rev. X **6**, 031039 (2016).

[45] R. Chao and B. W. Reichardt, npj Quantum Info. **4**, 1 (2018).

[46] L. B. Nguyen et al., PRX Quantum **3**, 037001 (2022).

[47] D. C. McKay, C. J. Wood, S. Sheldon, J. M. Chow, and J. M. Gambetta, Phys. Rev. A **96**, 022330 (2017).

[48] D. M. Abrams, N. Didier, B. R. Johnson, M. P. d. Silva, and C. A. Ryan, Nat. Electron. **3**, 744 (2020).

[49] A. Carignan-Dugas, J. J. Wallman, and J. Emerson, New J. Phys. **21**, 053016 (2019).

[50] F. Arute et al., Nature **574**, 505 (2019).

[51] S. T. Flammia and J. J. Wallman, ACM Trans. Quantum Comput. **1**, 1 (2020).

[52] A. Hashim et al., Phys. Rev. X **11**, 041039 (2021).

METHODS

Experimental setup

Extended Data Figure 1 shows the cryogenic setup and electronic wiring diagrams. The superconducting quantum processor used to perform the experiment is housed in a dilution refrigerator and operates at approximately 12 mK. The wiring is separated into two sides: the input side with predominantly attenuators, and the output side with mainly circulators and amplifiers. A combination of commercial K&L and in-house infrared Eccosorb® low-pass filters are added on both sides to mitigate high-frequency noise. The sample box is protected by tri-layer shields, with the copper shield further painted with *Berkeley black* mixture consisting of STYCAST 2850FT, silica, and carbon powder. The enclosure is made light-tight using indium seals. The parametric amplifier is placed inside a separate magnetic shield, and its pump line is also connected to low-pass filters to ensure suppression of high-frequency noise.

Due to resource constraint, only four qubits are connected to external circuitry during the experiment. All the input and output signals are diverted via directional couplers and power splitters to a spectrum analyzer for calibration. The pulses used to control the qubits are generated by an arbitrary waveform generator (AWG) at 1 GSa/s and upconverted using IQ mixers in combination with a local oscillator (LO) carrier tone. DC offsets using bias tees and local phases of the signals are calibrated to null carrier leakage. These offset parameters are found numerically by minimizing the signals at the carrier frequency using active feedback via the spectrum analyzer (SA) and COBYLA optimization.

The input signals are attenuated, filtered, and DC-blocked at room temperature to reduce noise inherent to electrical components inside the AWG. 26 dB of additional attenuation is added at the outputs of the AWG to fully utilize its dynamic range. The readout pulses are upconverted in a similar fashion. The upconversion circuit wiring is shown in the left panel of Extended Data Fig. 1c. While the qubits are manipulated via individual on-chip coplanar traces, the readout is performed in multiplexed fashion via a common bus. The microwave tones going into the fridge are checked using the SA for consistency.

The signal reflected from a readout resonator is circulated and amplified by a traveling wave parametric amplifier (TWPA) at the mixing chamber (MXC) plate, then by a high-electron-mobility-transistor (HEMT) amplifier at the 4-K plate, and finally by a room temperature amplifier before reaching the downconversion circuit. Here, an IQ mixer combines the same LO tone with the outgoing signal to produce an IF pulse that carries the information about the qubit. The measurement signal is further amplified at room temperature and goes through low-pass filters to suppress additional noise coming from the amplification. Finally, it is digitized at a rate of 1 GSa/s by an analog-to-digital converter (ADC) board attached directly to the PXI slot of the acquisition computer and demodulated via software. The downconversion circuit is shown in the right panel of Extended Data Fig. 1c. All electronic instruments are synchronized using a rubidium atomic clock. The components used to construct the experiment are listed in Extended Data Table I.
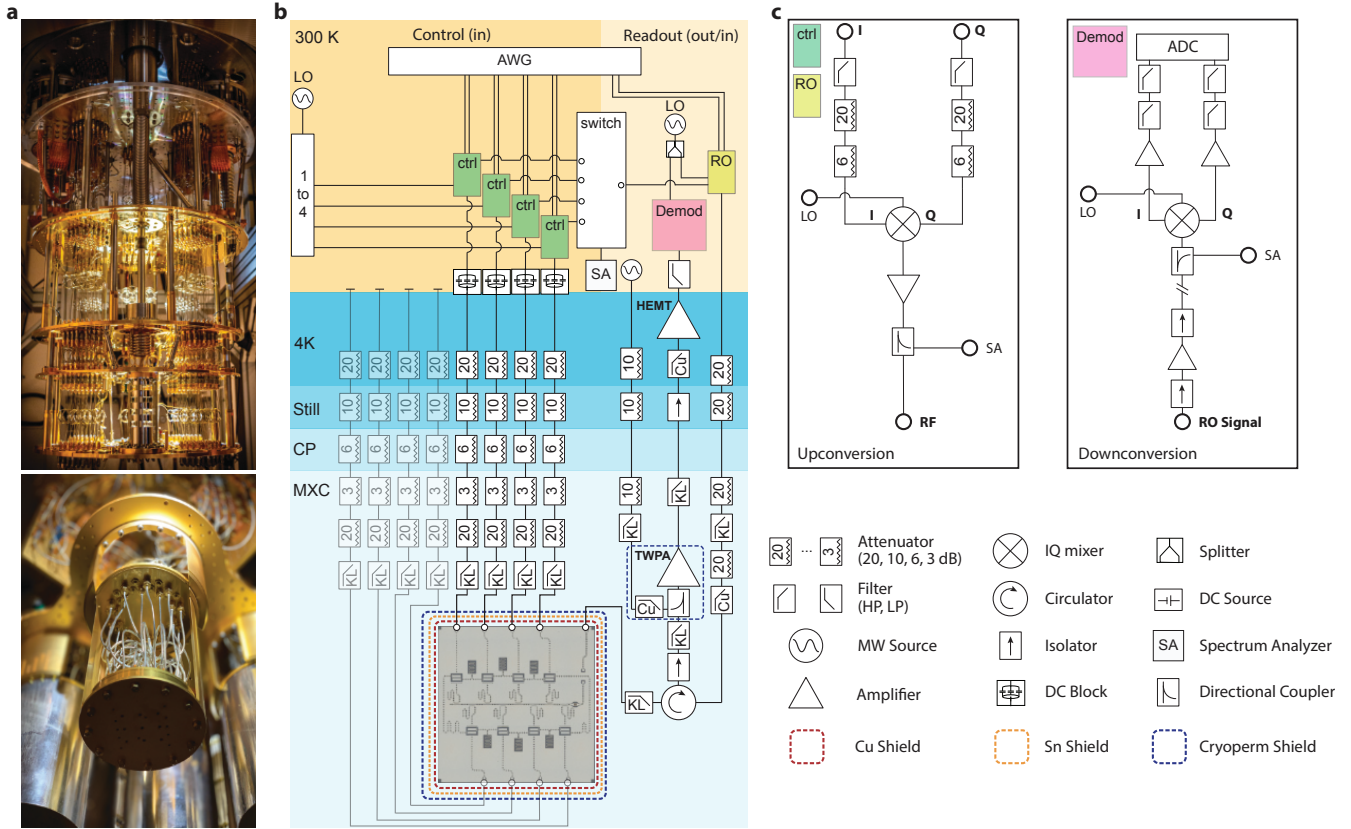
Device tuneup and characterization

The device used in this experiment consists of eight single-junction transmon qubits. Each is formed by two superconducting electrodes sandwiching a thin layer of aluminum oxide, resulting in a Josephson junction with Josephson energy E_J shunted by a capacitor with charging energy E_C. These characteristic energies define the spectrum of the qubit, resembling that of an anharmonic oscillator with transition frequency between the first two levels $\omega_{01}/2\pi \approx \sqrt{8E_J E_C} - E_C$ and anharmonicity $\alpha \approx -E_C$[14]. They are pairwise-coupled to mutual coplanar-waveguide (CPW) resonators (Fig. 1a), resulting in an effective capacitive coupling[29]. These couplers are designed to have frequencies at around 7 GHz and a resonator-qubit coupling strength of approximately 70 MHz. Each qubit is coupled to a separate control line and a CPW readout resonator. All readout resonators are coupled to a common bus which also serves as a Purcell filter.

The extracted parameters of the qubits and their readout used in this experiment are listed in Extended Data Table II. The readout and qubit frequencies are measured using microwave spectroscopy. The TWPA pump tone is calibrated using a vector network analyzer to optimize the signal-to-noise-ratio. The readout pulse is set to be 1-μs long, and its amplitude is adjusted to optimize the measurement fidelity $\mathcal{F}_{RO}(|i\rangle) = P(i|i)$, where $P(x|y)$ is the probability that the qubit initialized in state $|y\rangle$ is measured to be in state $|x\rangle$. The qubit-state-dependent readout signals are shown on the IQ planes in Extended Data Fig. 2a.

Component	Brand	Model
Dilution fridge	BlueFors	XLD
Control chassis	Keysight	PXI M9023A
AWG	Keysight	PXI M3202A
Digitizer	AlazarTech	ATS9373
LO RF source	Keysight	MXG N5183B
Spectrum analyzer	Keysight	N9320B
Frequency standard	SRS	FS725
Para. amplifier	MIT LL	TWPA
HEMT	LNF	LNC4_8C
TWPA pump	Hittite	HMC M2100
IQ mixer	Marki	MLIQ-0416
Bias-Tee	Mini-Circuits	ZX85-12G-S+
Attenuator	XMA	4882-6240
IR filter mixture	Laird	Eccosorb®CR-110

Extended Data Table I. Component brands and models used in the experimental setup.

Extended Data Fig. 1. **Experimental setup**. **a,** Dilution unit setup. **b,** Cryogenic wiring diagram. **c,** Room temperature control and readout circuitry.

The relaxation time T_1 and echo dephasing time T_2^E are extracted by applying a pulse sequence with variable length to the qubit, measuring the signal from the readout resonators, then fitting the data to appropriate functions with a decay parameter. Typical coherence time statistics consisting of ensembles of 100 individual measurements are shown in Extended Data Fig. 2**b**. We also measure the coherence statistics of the $|1\rangle \leftrightarrow |2\rangle$ transition for Q_3, with $\overline{T}_1^{(12)} = 46.96\ \mu s$ and $\overline{T}_2^{E,(12)} = 20.97\ \mu s$.
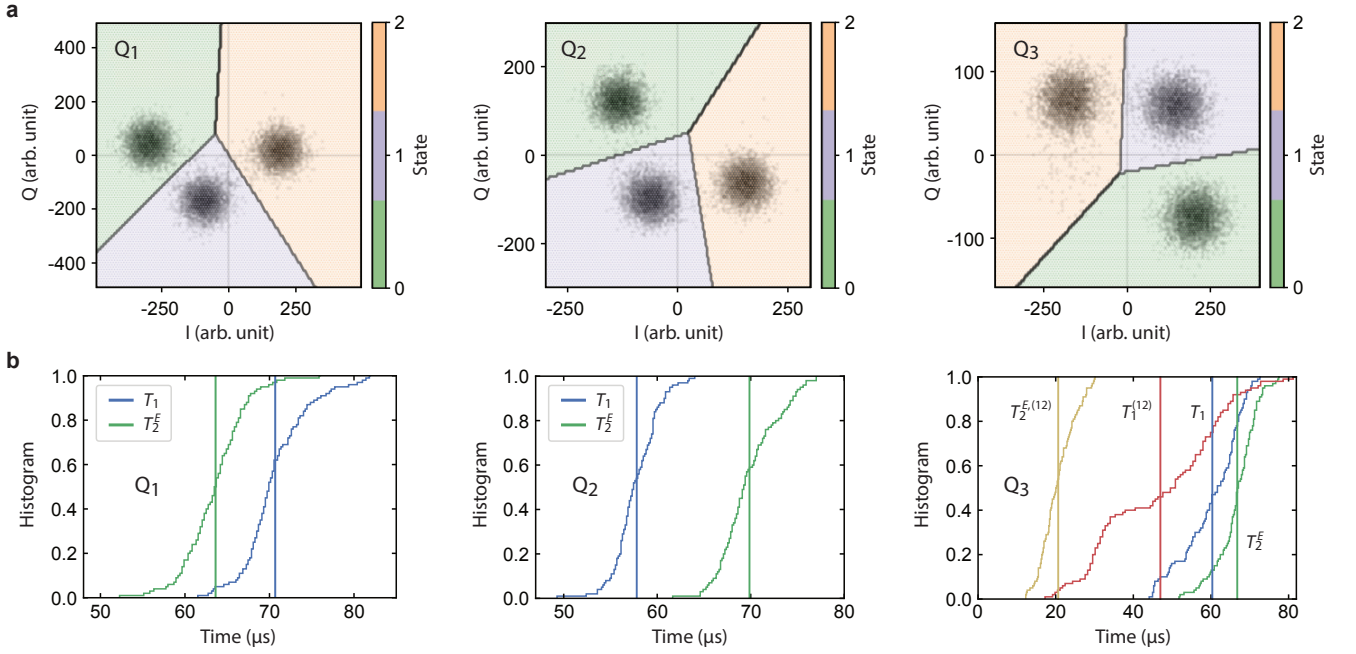
Single-qubit pulses have a Gaussian shape and are set to be 30-ns long. A series of Ramsey sequences is applied to extract the correct qubit frequencies. Their amplitudes are calibrated for $R_X(\pi/2)$ pulses by repeatedly applying even numbers of them up to $n_{pulse} = 200$ and measuring the outcomes to zero-in the correct parameters. By using the $R_X(\pi/2)$ gate in combination with virtual-Z gates, single qubit rotations can be implemented using the ZXZXZ decomposition[47], which significantly reduces the calibration time and complexity. Single-qubit gate fidelities extracted via streamline randomized benchmarking are included in Extended Data Table II.

Classical microwave crosstalk is present in the device and degrades its performance via two distinct processes. Firstly, an off-resonant microwave tone applied to the qubit slightly dresses its resonant frequency as discussed in the main text, leading to phase errors during execution of intended quantum circuits. Secondly, a leaked microwave tone applied to one qubit at the frequency of another qubit coupled to it induces a ZX interaction, which is commonly known as the cross-resonance effect, leading to spurious entanglement between the qubits. Thus, it is important to detect and suppress such crosstalk to improve chip-scale performance. To accomplish this, additional microwave tones are applied simultaneously to neighboring qubits during the gate operation of the intended qubits. Their amplitudes and phases are tuned up to destructively interfere with the crosstalk tones. The parameters are further optimized using covariance ma-

	Q_1	Q_2	Q_3
$\omega_{01}/2\pi$ (GHz)	5.23	5.32	5.44
α (GHz)	-0.26	-0.27	-0.27
$\omega_{RO}/2\pi$ (GHz)	6.23	6.32	6.44
$\overline{T}_1$ (μs)	70.67	57.81	60.35
$\overline{T}_2^E$ (μs)	63.62	69.87	66.77
$\mathcal{F}_{RO}$ ($|0\rangle$)	99.6%	99.3%	99.1%
$\mathcal{F}_{RO}$ ($|1\rangle$)	98.2%	97.4%	97.5%
$\mathcal{F}_{RO}$ ($|2\rangle$)	96.8%	96.8%	95.8%
$\mathcal{F}_{1Q}$ (isolated)	99.88(1)%	99.85(1)%	99.80(1)%
$\mathcal{F}_{1Q}$ (joint)	99.68(1)%	99.4(1)%	99.72(3)%

Extended Data Table II. Relevant device parameters.

Extended Data Fig. 2. Device characterization. a, Dispersive readout histogram showing the IQ signal of the resonators corresponding to the qubits in state $|0\rangle$, $|1\rangle$, and $|2\rangle$. **b,.** Coherence statistics acquired continuously for 100 iterations. The vertical lines indicate their average values.

trix adaptation (CMA) with simultaneous randomized benchmarking. Typically, the simulatenous single-qubit gate errors are considerably higher than the isolated errors (Extended Data Table II). Although we routinely observe high isolated single-qubit gate fidelities immediately following a calibration round, the simultaneous fidelities tend to saturate toward the reported numbers, which are more relevant for the present experiment.

Using optimal readout and single-qubit gate parameters, a readout confusion matrix is extracted for each qubit by preparing it in a certain state and measuring the probability for it to be in $|0\rangle$, $|1\rangle$, or $|2\rangle$ states. This results in a matrix that is ideally diagonal with entries equal to 1. Thus, a correction matrix can be found by inverting the confusion matrix. The correction matrix is subsequently applied to all measurement outcomes to compensate for readout errors.

Floquet states and quasienergies

We consider a periodically driven qubit system described by the Hamiltonian

$$\hat{\mathcal{H}}_{\mathrm{q}}(t)/\hbar = -\frac{\omega_{\mathrm{q}}}{2}\hat{\sigma}_{\mathrm{z}} + A\cos(\omega_{\mathrm{d}}t + \varphi)\hat{\sigma}_{\mathrm{x}}. \tag{5}$$

For a Hamiltonian with a period of $T = 2\pi/\omega_{\mathrm{d}}$, we can find a time-periodic Floquet state, $|u(t)\rangle_{\mathrm{F}} = |u(t+T)\rangle_{\mathrm{F}}$, with quasienergy $\hbar\varepsilon$ through the Floquet equation,

$$\left(\hat{\mathcal{H}}_{\mathrm{q}}(t) - i\hbar\partial_t\right)|u(t)\rangle_{\mathrm{F}} = \hbar\varepsilon|u(t)\rangle_{\mathrm{F}}. \tag{6}$$

Note that this equation is connected to the Schrödinger equation via the relation $|u(t)\rangle_{\mathrm{F}} = e^{i\varepsilon t}|\psi(t)\rangle$. To find

the solutions of Eq. (6), we write the Floquet state as a Fourier series comprising of time-independent states $|u^k\rangle$, where k is an integer,

$$|u(t)\rangle_{\mathrm{F}} = \sum_k e^{ik\omega_{\mathrm{d}}t}|u^k\rangle, \tag{7}$$

and then inserting it into the Floquet equation. By grouping terms which have the same Fourier frequencies, we can obtain $\varepsilon|u^k\rangle = (-\frac{\omega_{\mathrm{q}}}{2}\hat{\sigma}_{\mathrm{z}} + k\omega_{\mathrm{d}})|u^k\rangle + e^{i\varphi}\frac{A}{2}\hat{\sigma}_{\mathrm{x}}|u^{k-1}\rangle + e^{-i\varphi}\frac{A}{2}\hat{\sigma}_{\mathrm{x}}|u^{k+1}\rangle$. Under the conditions $A \ll \omega_{\mathrm{q}}, \omega_{\mathrm{d}}$ and $\omega_{\mathrm{q}} \leq 2\omega_{\mathrm{d}}$, this can be put into the matrix form,

$$\begin{bmatrix} -\frac{\omega_{\mathrm{q}}}{2}\hat{\sigma}_{\mathrm{z}} + k\omega_{\mathrm{d}} & e^{i\varphi}\frac{A}{2}\hat{\sigma}_{\mathrm{x}} \\ e^{-i\varphi}\frac{A}{2}\hat{\sigma}_{\mathrm{x}} & -\frac{\omega_{\mathrm{q}}}{2}\hat{\sigma}_{\mathrm{z}} + (k-1)\omega_{\mathrm{d}} \end{bmatrix}\begin{bmatrix} |u^k\rangle \\ |u^{k-1}\rangle \end{bmatrix} = \varepsilon\begin{bmatrix} |u^k\rangle \\ |u^{k-1}\rangle \end{bmatrix}. \tag{8}$$

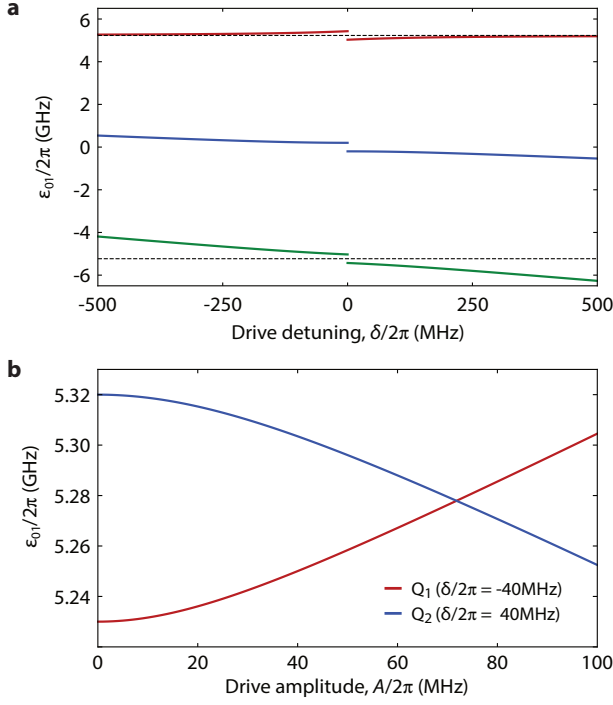Its eigenstates yield the Floquet basis states using Eq. (7),

$$|u_+(t)\rangle_{\mathrm{F}} \propto \left(\delta + \sqrt{A^2 + \delta^2}\right)|0\rangle + e^{-i(\omega_{\mathrm{d}}t+\varphi)}A|1\rangle,$$
$$|u_-(t)\rangle_{\mathrm{F}} \propto \left(\delta - \sqrt{A^2 + \delta^2}\right)|0\rangle + e^{-i(\omega_{\mathrm{d}}t+\varphi)}A|1\rangle, \tag{9}$$

and its eigenvalues give the quasienergies of $e^{ik\omega_{\mathrm{d}}t}|u_\pm(t)\rangle_{\mathrm{F}}$ as

$$\varepsilon_\pm^k = \left(k - \frac{1}{2}\right)\omega_{\mathrm{d}} \pm \frac{1}{2}\sqrt{A^2 + \delta^2}, \tag{10}$$

where $\delta = \omega_{\mathrm{d}} - \omega_{\mathrm{q}}$ is the drive detuning. In this work, we allocate the index of the Floquet basis to match with that of the bare basis, i.e., $|\langle n|u_n(t)\rangle_{\mathrm{F}}|^2 > 0.5$.

Extended Data Fig. 3. **Floquet quasienergies**. **a,** Transition energies between $|u_0(t)\rangle_F$ and $|u_1(t)\rangle_F$ with drive amplitude 200 MHz, qubit frequency 5.23 GHz, and varying drive detuning δ. The dashed lines represent the qubit frequency. **b,** Dependence of ε_{01} on the drive amplitude. By driving qubit $Q_1(Q_2)$ with red(blue) detuned microwave, two qubits can be brought into resonance.

Specifically, if $\delta > 0$, we define $|u_{+(-)}(t)\rangle_F$ as $|u_{0(1)}(t)\rangle_F$ and $\varepsilon_{+(-)}$ as $\varepsilon_{0(1)}$, otherwise the index is inverted. Thus, the quasienergy difference, $\varepsilon_{01} \equiv \varepsilon_1 - \varepsilon_0$, abruptly changes at $\delta = 0$ (Extended Data Fig. 3**a**).

Heisenberg interactions between Floquet states
As described by Eq. (4), the interaction strengths of the Floquet-engineered Heisenberg Hamiltonian are given as

$$J_{XY} = J\langle c_{01}^{(1)} c_{10}^{(2)} \rangle_t = J\langle c_{10}^{(1)} c_{01}^{(2)} \rangle_t,$$
$$J_{ZZ} = J\langle c_{11}^{(1)} c_{11}^{(2)} + c_{00}^{(1)} c_{00}^{(2)} - c_{00}^{(1)} c_{11}^{(2)} - c_{11}^{(1)} c_{00}^{(2)} \rangle_t, \quad (11)$$

where $c_{ab}^{(n)} = \langle \psi_a^{(n)}(t)|\hat{\sigma}_x^{(n)}|\psi_b^{(n)}(t)\rangle$ is for qubit Q_n and $\langle ... \rangle_t$ denotes the time-average value. For the transverse (XY) spin-exchange interaction, we drive $Q_1(Q_2)$ with red(blue) detuned microwaves to bring their quasienergy differences $\varepsilon_{01}^{(n)}$ into resonance. Specifically, this condition is satisfied for quasienergy transitions $e^{ik\omega_d^{(n)}t}|u_0^{(n)}(t)\rangle_F \leftrightarrow e^{i(k+1)\omega_d^{(n)}t}|u_1^{(n)}(t)\rangle_F$ when mapped by a certain drive amplitude (Eq. (10) and Extended Data Fig. 3**b**). Accordingly, the Floquet states' coefficients read

$$c_{01}^{(1)} = \langle \psi_0^{(1)}(t)|\hat{\sigma}_x^{(1)}|\psi_1^{(1)}(t)\rangle$$
$$= e^{-i\varepsilon_{01}^{(1)}t}\langle u_-^{(1)}(t)|_F\hat{\sigma}_x^{(1)}e^{i\omega_d^{(1)}t}|u_+^{(1)}(t)\rangle_F \quad (12)$$

and

$$c_{10}^{(2)} = \langle \psi_1^{(2)}(t)|\hat{\sigma}_x^{(2)}|\psi_0^{(2)}(t)\rangle$$
$$= e^{i\varepsilon_{01}^{(2)}t}\langle u_-^{(2)}(t)|_F e^{-i\omega_d^{(2)}t}\hat{\sigma}_x^{(2)}|u_+^{(2)}(t)\rangle_F. \quad (13)$$

When the blue- and red-detuned drives have the same detuning $|\delta|$ and amplitude A, the time-average XY interaction strength is obtained as

$$|J_{XY}| = J|\langle c_{01}^{(1)} c_{10}^{(2)}\rangle_t| = J\frac{(|\delta| + \sqrt{A^2 + \delta^2})^2}{4(A^2 + \delta^2)}, \quad (14)$$

using Eq. (9). On the other hand, the relevant coefficients for the longitudinal (ZZ) spin-spin interaction read

$$c_{\pm\pm}^{(n)} = \langle u_\pm^{(n)}(t)|_F\hat{\sigma}_x^{(n)}|u_\pm^{(n)}(t)\rangle_F$$
$$= \frac{A_n(\delta_n \pm \sqrt{A_n^2 + \delta_n^2})\cos\left(\omega_d^{(n)}t + \varphi_n\right)}{A_n^2 + \delta_k\left(\delta_n \pm \sqrt{A_n^2 + \delta_n^2}\right)}. \quad (15)$$

When the microwave drives for Q_1 and Q_2 are both detuned to red or blue,

$$c_{11}^{(1)} c_{11}^{(2)} + c_{00}^{(1)} c_{00}^{(2)} - c_{11}^{(1)} c_{00}^{(2)} - c_{00}^{(1)} c_{11}^{(2)}$$
$$= c_{++}^{(1)} c_{++}^{(2)} + c_{--}^{(1)} c_{--}^{(2)} - c_{++}^{(1)} c_{--}^{(2)} - c_{--}^{(1)} c_{++}^{(2)}$$
$$= \frac{4A_1A_2\cos\left(\omega_d^{(1)}t + \varphi_1\right)\cos\left(\omega_d^{(2)}t + \varphi_2\right)}{\sqrt{(A_1^2 + \delta_1^2)(A_2^2 + \delta_2^2)}}. \quad (16)$$
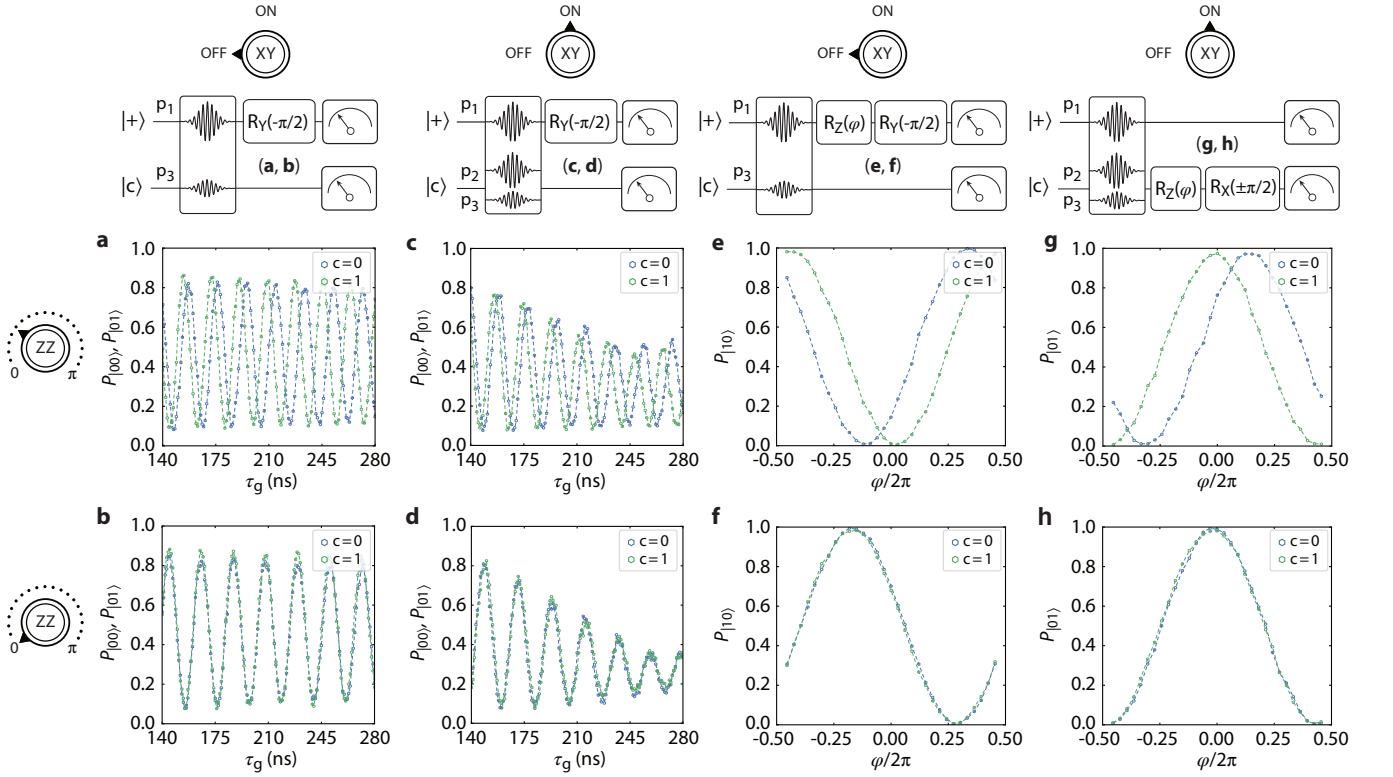
For $\omega_d^{(1)} = \omega_d^{(2)}$, the time-averaged ZZ interaction strength is thus given as

$$J_{ZZ} = J\langle c_{11}^{(1)} c_{11}^{(2)} + c_{00}^{(1)} c_{00}^{(2)} - c_{00}^{(1)} c_{11}^{(2)} - c_{11}^{(1)} c_{00}^{(2)}\rangle_t$$
$$= J\frac{2A_1A_2\cos(\varphi_1 - \varphi_2)}{\sqrt{(A_1^2 + \delta_1^2)(A_2^2 + \delta_2^2)}}. \quad (17)$$

ZZ interaction measurements
The ZZ rate can be estimated using a time-efficient and reliable Ramsey-like experiment. The sequence consists of initializing one qubit in a superposition state, then applying the intended pulses and measuring it along the Z axis. The Z rotation resulting from the frame frequency difference between the bare qubit and the Floquet qubit manifests as an oscillation of the qubit's population with respect to the pulse duration. For a finite spin-spin coupling, the two oscillation frequencies corresponding to the other qubit in the ground and excited states are subtracted to find the ZZ rate. As this always works for both zero and finite XY coupling (Extended Data Fig. 4**a-d**), it is a versatile method to approximate the longitudinal coupling. However, its accuracy is limited by the fast oscillations and subsequently the fitting errors.

To accurately measure the ZZ angle at the end of a pulse with a fixed duration τ_g, a sequence with the addition of a single-qubit Z gate with a variable phase φ is used. The measured qubit population depends on φ, and Φ_{ZZ} is the phase difference corresponding to the other

Extended Data Fig. 4. **Spin-spin interaction measurement**. **a-d,** Dependence of Q_1's Z rate on Q_2's state, with transverse coupling off (**a-b**) and on (**c-d**). **e-f,** Dependence of Q_1's Z phase on Q_2's state, without transverse coupling. The phase difference results from Φ_{ZZ}. **g-h,** When the two-qubit states $|10\rangle$ and $|01\rangle$ are swapped via XY coupling, the sequence instead includes the projection gate on Q_2. The angle polarity is chosen according to the initial control state. The analysis takes into account the 2π phase difference between the curves when $\Phi_{ZZ} = 0$ to mimic the result without transverse coupling.

qubit being in $|0\rangle$ and $|1\rangle$ states (Extended Data Fig. 4**e-f**). The measurement also works when there is a complete population swap between $|10\rangle$ and $|01\rangle$. In this case, the Z gate is applied to the other qubit instead, with the projection gate's polarity depending on its initial state. $\Phi_{ZZ} = 0$ then corresponds to the phase difference of 2π, which can be subtracted from the results to give overlapping trajectories for zero ZZ coupling. We note that since the qubit is expected to be in the ground state if there is no phase gate induced by the pulse, a similar approach is used to calibrate single-qubit Z gates. Finally, the method can be extended to analyze a three-qubit CCZ entanglement.

For simultaneous transverse coupling resulting in arbitrary swapping angle, we find tomographic reconstruction to be the most reliable. In this approach, quantum state tomography and quantum process tomography are performed to find the state or process matrices resulting from the applied gate. An optimization routine is then utilized to extract the swapping (XY) and ZZ angles. The accuracy of this method is inherently limited by the SPAM errors of the tomography procedures.

Two-qubit gate calibration

The programmable interactions can be employed to im-

plement two-qubit gates in a straightforward manner. Since the XY and ZZ operations commute, we can decompose the Heisenberg unitary as $\hat{U}_{XXZ}(\Theta_{XY}, \Phi_{ZZ}) = e^{-i\hat{\mathcal{H}}_{XXZ}t/\hbar} = \hat{U}_{XY}(\Theta_{XY}) \times \hat{U}_{ZZ}(\Phi_{ZZ})$, where

$$
\hat{U}_{XY}(\Theta_{XY}) = \exp\left[-i\frac{\Theta_{XY}}{2}(\hat{X}\hat{X} + \hat{Y}\hat{Y})\right]
$$
$$
= \begin{pmatrix} 1 & 0 & 0 & 0 \\ 0 & \cos(\Theta_{XY}) & -i\sin(\Theta_{XY}) & 0 \\ 0 & -i\sin(\Theta_{XY}) & \cos(\Theta_{XY}) & 0 \\ 0 & 0 & 0 & 1 \end{pmatrix} \quad (18)
$$

and

$$
\hat{U}_{ZZ}(\Phi_{ZZ}) = \exp\left[-i\frac{\Phi_{ZZ}}{2}\hat{Z}\hat{Z}\right]
$$
$$
= \begin{pmatrix} e^{-i\Phi_{ZZ}/2} & 0 & 0 & 0 \\ 0 & e^{i\Phi_{ZZ}/2} & 0 & 0 \\ 0 & 0 & e^{i\Phi_{ZZ}/2} & 0 \\ 0 & 0 & 0 & e^{-i\Phi_{ZZ}/2} \end{pmatrix}.
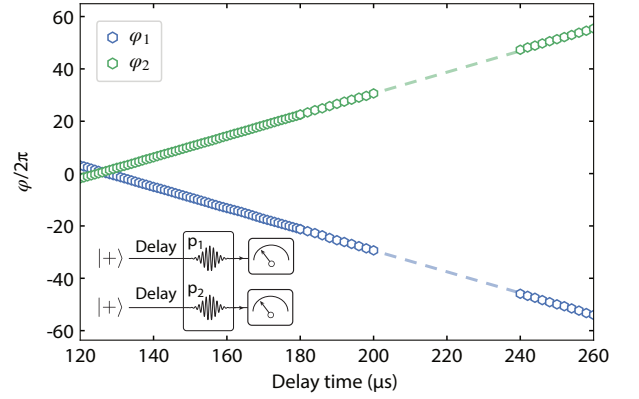$$
$$(19)$$

Naturally, the coherent flip-flop between $|10\rangle$ and $|01\rangle$ in Fig. 2**b** is equivalent to the rotation of the transverse coupling angle Θ_{XY}, with $\Theta_{XY} = \pi/2$ corresponding to a full swap (the oscillation angle is

2Θ_XY). The measured longitudinal coupling angle Φ_{ZZ} in Fig. 2c illustrates a control-phase entangling operation up to local Z rotations, with $\Phi_{\text{ZZ}} = \pi/2$ corresponding to a CZ gate following the relation $\hat{U}_{\text{CZ}} = \exp\left[-i\pi(\hat{Z}\hat{Z} + \hat{I}\hat{I} - \hat{Z}\hat{I} - \hat{I}\hat{Z})/4\right]$. Therefore, two-qubit gates can be calibrated up to local Z gates using the observed interactions. Notably, the realized iSWAP and SWAP gates arise directly from the XX and isotropic XXX Heisenberg models, while the CZ gate results from the pure spin-spin coupling of the transverse-field Ising model. In sum, the realized Floquet system can be used as a robust quantum many-body simulator with high-fidelity gates as consequences.

With the connection between different interaction models and gate unitaries established, the presented gates are calibrated as follows. (i) First, a frequency sweep using a large-amplitude microwave pulse is performed to exclude spectrally crowded regions. (ii) The pulses are applied at the appropriate frequencies, with p_1 and p_2 facilitating the transverse coupling, while p_1 and p_3 inducing the longitudinal coupling. (iii) A complete swap angle $\Theta_{\text{XY}} = \pi/2$ and zero ZZ angle, $\Phi_{\text{ZZ}} = 0$, (cf. Fig. 2) correspond to an iSWAP gate, up to local Z gates. The measurement can be performed with the intended gate repeated for an odd number of times, amplifying coherent errors, to find the correct pulse parameters. (iv) With p_2 off, there is no transverse coupling, and p_3 can be tuned to get $\Phi_{\text{ZZ}} = \pi/2$, giving the CZ gate. (v) With p_1 and p_2 calibrated to give a complete population swap, p_3 can be tuned to get $\Phi_{\text{ZZ}} = \pi/2$, giving the SWAP gate. (vi) The local phase gates are implemented in software by tracking the frame of the qubit and imparting relative phases on subsequent single-qubit pulses. Their angles are calibrated via least square optimization using tomographic measurement of the final states. Using these calibration steps, we realized a 230-ns-long iSWAP gate with $\{A_1, A_2, A_3\}/2\pi = \{71.7, 65.2, 21.35\}$ MHz, a 180-ns-long CZ gate with $\{A_1, A_3\}/2\pi = \{71.2, 28.5\}$ MHz, and a 260-ns-long SWAP gate with $\{A_1, A_2, A_3\}/2\pi = \{96.9, 28.5, 14.2\}$ MHz. As Q_3's $|1\rangle \leftrightarrow |2\rangle$ frequency is close to that of Q_1's $|0\rangle \leftrightarrow |1\rangle$, we implemented the CZ gate by applying p_1 and p_3 at a frequency 40 MHz blue-detuned from Q_1 to avoid any spectator leakage error.

Dynamical phase and Z gates

In general, integrating a gate resulting from the transverse coupling into a quantum circuit must overcome two technical requirements. First, while the XY interaction is facilitated between the Floquet qubits in the dressed frame, the measurements and single-qubit gates are performed on the bare qubits with different transition frequencies. This leads to an accumulation of single-qubit phases that depend on the time at which the gate is applied, and the accumulation rate is equal to the difference in qubit frequencies[48]. To verify this effect, we apply

Extended Data Fig. 5. **Dynamical phase accumulation**. After preparing the qubits in the superposition state $(|0\rangle + |1\rangle) \otimes (|0\rangle + |1\rangle)/2$, calibrated pulses are employed to facilitate $|10\rangle$ and $|01\rangle$ coherent exchange (inset). Tomographic measurement reveals the qubits' Z phases which are linearly dependent on the time at which the swap pulses are applied.

pulses p_1 and p_2 calibrated to implement a perfect swap, then measure the local Z phases $\varphi_{1,2}$ of the qubits. Upon sweeping the delay time before applying the pulses, we find these phases to increase linearly, and the extracted slope is, within measurement uncertainty, the same as the qubits' frequency difference, as shown in Extended Data Fig. 5. Including other gates before this transverse swap has the same effect (gap between the data points). Thus, the Z gate corrections must take this dynamics into account.

Second, the ZXZXZ single-qubit gate decomposition using virtual-Z gates comes with the following caveats. This scheme realizes arbitrary single-qubit rotation via Euler decomposition[47],

$$\hat{U}(\theta, \phi, \lambda) = \hat{R}_{\text{Z}}(\phi)\hat{R}_{\text{X}}(\theta)\hat{R}_{\text{Z}}(\lambda) \qquad (20)$$
$$= \hat{R}_{\text{Z}}\left(\phi - \frac{\pi}{2}\right)\hat{R}_{\text{X}}\left(\frac{\pi}{2}\right)\hat{R}_{\text{Z}}(\pi - \theta)\hat{R}_{\text{X}}\left(\frac{\pi}{2}\right)\hat{R}_{\text{Z}}\left(\lambda - \frac{\pi}{2}\right).$$

Here, the Z rotation is implemented virtually by keeping track of all the physical single-qubit X gates and redefining the rotation axes for all the gates following an intended Z gate, a procedure known as *phase carrying*. A compatible two-qubit unitary must therefore be a *phase carrier*. This procedure thus breaks down when there is an energy exchange gate in the circuit, for instance, $\sqrt{\text{iSWAP}}$. In addition, since $\hat{X}\hat{X}$ and $\hat{Y}\hat{Y}$ do not commute with single-qubit $\hat{Z}$, it is problematic to implement virtual-Z gates in the circuit to correct for the additional single-qubit Z phases induced during the operations[35].

In this work, we utilize the special property of the swap angle $\Theta_{\text{XY}} = \pi/2$, $(\hat{R}_{\text{Z}}(\varphi_1) \otimes \hat{R}_{\text{Z}}(\varphi_2)) \times \hat{U}_{\text{XXZ}}(\pi/2, \Phi_{\text{ZZ}}) = \hat{U}_{\text{XXZ}}(\pi/2, \Phi_{\text{ZZ}}) \times (\hat{R}_{\text{Z}}(\varphi_2) \otimes \hat{R}_{\text{Z}}(\varphi_1))$, to compile the quantum circuits. The induced Z phases occured during the gate operations can also be corrected by applying virtual-Z gates afterward[48]. The circuit compilation thus requires two additional steps at each iSWAP or SWAP cycle, which can be satisfied
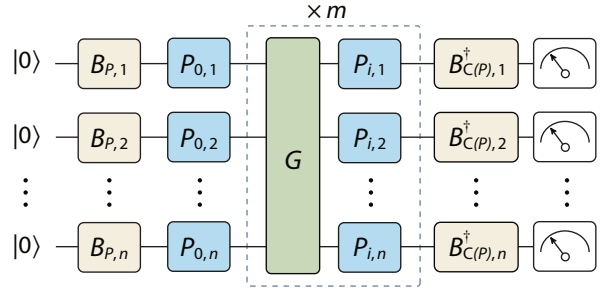
by computing and adding virtual-Z gates after them: (i) correction gates for Z phases must account for the dynamical phase accumulation due to the frame difference, and (ii) the phase tracking for virtual-Z gates must switch the frames. In practice, condition (i) only requires accounting for the time interval between consecutive gates, and condition (ii) is fulfilled by adding/subtracting the carrying phase, which is an internal part of the compilation software. We note that SU(2) compilations that are compatible with any two-qubit gate have been recently introduced[35], so other gates in the XY family are in principle fully compatible with any platform supporting native virtual-Z gates.

CCZ gate calibration

Three different gates must be calibrated for the CCZ sequence: (i) a $|11\rangle_c \leftrightarrow |02\rangle_c$ iSWAP gate between Q_2 and Q_3 that does not induce any spectator ZZ error between Q_1 and Q_2, (ii) a CZ gate between Q_1 and Q_2 that does not induce any spectator error, as this can lead to an effective ZZ entanglement after the shelving for control state $|11\rangle_c$, and (iii) a CPhase gate at the end to ensure an overall identity operation on Q_2 and Q_3, which must not induce extraneous ZZ between Q_1 and Q_2. We tune up these gates as follows.

Similar to XY gates between the computational levels, a frequency sweep is performed to find an appropriate detuning from Q_3's $|1\rangle \leftrightarrow |2\rangle$ transition. A single drive tone is then applied to Q_3 at this frequency, its duration and amplitude are varied until a good $|11\rangle_c \leftrightarrow |02\rangle_c$ chevron pattern is observed. The ZZ angle between Q_1 and Q_2 is measured at the end of the pulse and then cancelled by applying an additional pulse on Q_1. It is important to completely cancel this spurious coupling, since its presence results in a non-zero ZZ phase between Q_1 and Q_2 for the control state $|11\rangle_c$, rendering the shelving scheme ineffective. We found the best detuning to be 22 MHz below Q_3's $|1\rangle \leftrightarrow |2\rangle$ transition, and optimal pulse duration to be 280 ns with a ramping time of 120 ns. Similarly, a pulse on Q_3 is added during the CZ gate operation on Q_1 and Q_2 to null any spurious effect on the shelved state. To satisfy the more stringent requirements, we increase the ramping time to 90 ns and gate time to 210 ns.

After applying three pulses consecutively, the residual conditional phase Φ_{ZZ} between Q_2 and Q_3 is measured. We then apply a CPhase gate between them to invert this conditional phase, and at the same time cancel the residual ZZ coupling between Q_1 and Q_2. To satisfy the requirements, the gate consists of three microwave pulses applied to all three qubits. The pulses on Q_2 and Q_3 are tuned up first to negate all the entanglement between them. Then, the remaining ZZ phase between Q_1 and Q_2 is cancelled by applying a small-amplitude pulse to Q_1. The tuned up CPhase gate is 180-ns long, with a ramp time of 80-ns, bringing the total sequence duration to 950-ns. The calibration is performed manually in this simple fashion, so we expect even better gate performance with future optimization.

Extended Data Fig. 6. **Cycle benchmarking sequence**. The sequence consists of a cycle of preparation gates B_P, followed by a cycle of Pauli gate P. The gate of interest G is interleaved between cycles of randomly-sampled Pauli gates for m different iterations. Finally, the qubits are rotated to the original eigenstates via a cycle of $B^\dagger_{C(P)}$'s. A reference sequence has the identity gate replacing the G cycle.
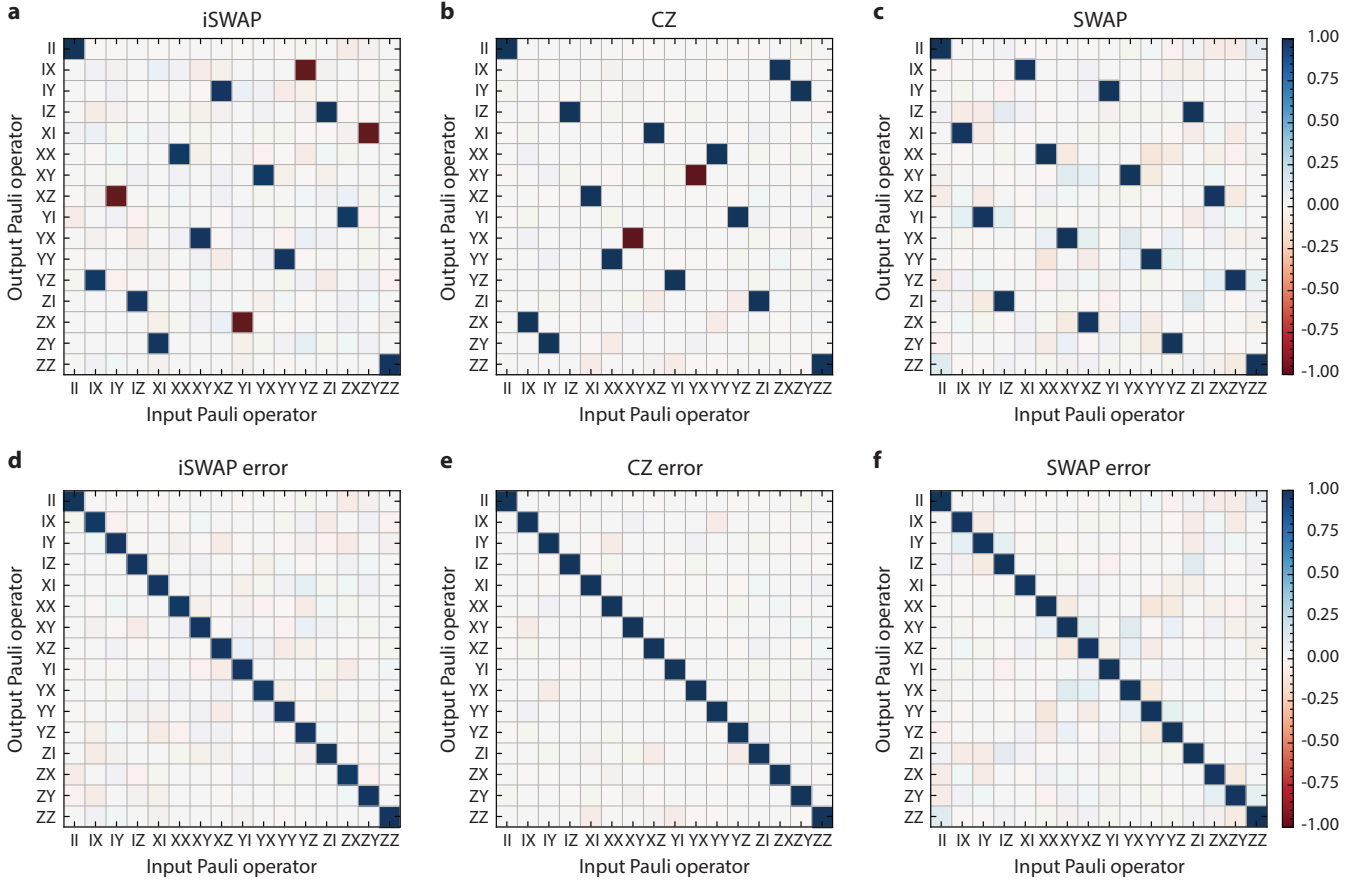
Cycle benchmarking

Cycle benchmarking (CB)[33] is a scalable benchmarking protocol for characterizing errors and noise in cycles containing parallel gate operations. Unlike randomized benchmarking (RB), which tailors all errors into a global depolarizing channel via Clifford twirling, CB tailors all errors into stochastic Pauli channels via Pauli twirling. To measure the errors for a Pauli channel $P \in \{I, X, Y, Z\}^{\otimes n}$ for a cycle of operations containing n qubits, the register of qubits is first prepared in an eigenstate of P via single-qubit basis operations B_P, followed by a cycle of randomly-sampled Pauli gates P, after which the cycle or gate of interest G is interleaved between alternating cycles of randomly-sampled Pauli gates for m iterations, and finally the register of qubits is rotated back to the eigenstate of P via refocusing gates $B^\dagger_{C(P)}$. Each Pauli channel P is fitted to an exponential decay function $A_P f_P^m$ for a circuit depth m, where the fidelity of each Pauli channel,

$$f_P = \text{Tr}\Big[C(P)^\dagger \tilde{C}(\rho)\Big], \tag{21}$$

is captured by the overlap of the results of the ideal circuit $C(P)$ with the noisy implementation $\tilde{C}(\rho)$, where ρ represents the initial state of the n-qubit system in a $+1$-eigenstate of P; the constant A_P represents the state preparation and measurement (SPAM) error. By measuring the performance of the interleaved gate cycle G at two different circuit depths $\{m_1, m_2\}$ for K different Pauli channels, one may estimate the process fidelity via

$$\mathcal{F}_p = \frac{1}{K} \sum_{P \in \mathbb{P}} \left(\frac{\sum_{l=1}^L f_{P,m_2,l}}{\sum_{l=1}^L f_{P,m_1,l}} \right)^{\frac{1}{m_2 - m_1}}, \tag{22}$$

where $\sum_{l=1}^L$ represents the sum over the L different randomizations for each Pauli channel P, and $\frac{1}{K}\sum_{P \in \mathbb{P}}$ represents the average over all measured Pauli channels.

Extended Data Fig. 7. **Quantum process tomography results**. Experimentally obtained PTM's corresponding to **a,** iSWAP, **b,** CZ, and **c,** SWAP gates. Their ideal counterparts are used to compute the respective error PTMs (panels **d-f**).

Here, $\mathbb{P}$ is a subset of the n-qubit Pauli group that has been sampled from the full set of 4^n possible channels. The number of different Pauli channels $K = |\mathbb{P}| \leq 4^n$ sets the precision of the fidelity estimate[33]. The process infidelity is given as $e_\mathrm{p} = 1 - \mathcal{F}_\mathrm{p}$.

Much like interleaved RB (IRB), which measures the fidelity of a dressed gate composed of the interleaved gate G with a cycle of random Clifford gates, CB measures the fidelity of a dressed cycle composed of the interleaved cycle G and a cycle of random Pauli gates. Similar to IRB, one can estimate the average gate infidelity of just the interleaved cycle G by taking the ratio of the process fidelities of the dressed D and reference R cycles,
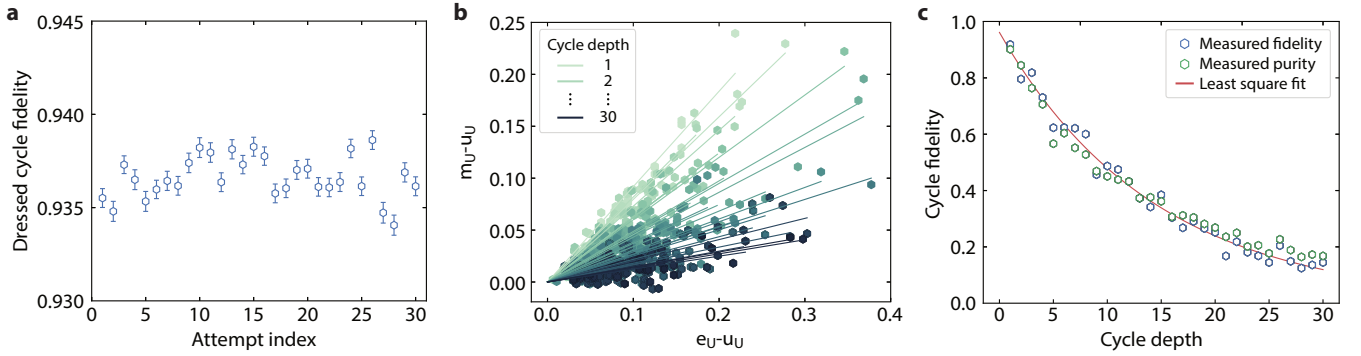
$$e_\mathrm{g} = \frac{d-1}{d}\left(1 - \frac{\mathcal{F}_\mathrm{p}^D}{\mathcal{F}_\mathrm{p}^R}\right), \qquad (23)$$

where $d = 2^n$ is the dimension of the Hilbert space for n qubits. It should be noted that estimating the isolated gate fidelity via IRB or CB can be subjected to large systematic bounds, with upper and lower bounds that may differ by orders of magnitude depending on the unitarity of the gate or cycle[49]. However, it has been shown that CB tightens the upper- and lower-bounds on the fidelity estimate relative to IRB[20], due to the fact

that random Pauli gates are more efficiently decomposed into native operations than random Clifford gates. We note that since the conditions of the qubits, including coherence times, naturally fluctuate, while the cycles of interest are not measured simultaneously, Eq. (23) should be viewed as an estimation.

Cross-Entropy Benchmarking

Cross Entropy Benchmarking (XEB)[50] is an additional SPAM-free method we leverage for studying the errors and noise associated with the three-qubit CCZ gate. XEB benefits from being able to benchmark non-Clifford unitaries and was instrumental in the first experimental demonstration of quantum advantage. In the XEB protocol, the errors of a multi-qubit gate are tailored into a global depolarizing channel via interleaved cycles of randomly chosen local $SU(2)$ gates. Given sufficient tailoring of the noise, one expects to observe scrambling behavior that manifests as the distribution of probabilities p for observing a particular bitstring following the Porter-Thomas distribution $P(p) = (d-1)(1-p)^{d-2}$, where $d = 2^n$ is the dimension of the measured Hilbert space. For a sufficiently randomized circuit, the circuit error can be conveniently thought of as the deviation of

Extended Data Fig. 8. **Extended verification of CCZ**. **a,** Fluctuation of the dressed process fidelity given by CB over a time span of eight hours. **b,** XEB circuit fidelity at different cycle depths. **c,** The overall decrease of the average XEB circuit fidelity at larger depths reveals the estimated dressed process fidelity of 93.3(2)%. Note that these fidelities include the errors from single-qubit gates used to construct random cycles. We additionally extract the speckle purity at each cycle depth, which is close to the cycle fidelity.

the measured bitstring distributions from a uniform distribution.

We seek to make this relationship precise. We denote all possible bitstrings as x_i for $i = 1, ..., 2^n$ where n is the number of qubits that the unitary of interest act on. We assign $q(x_i)$ as the measured distribution, and define the linear cross-entropy between two probability distributions $p_1(x)$ and $p_2(x)$ as

$$H(p_1, p_2) = \sum_x p_1(x)p_2(x), \qquad (24)$$

where the sum runs over the full support of the probability distributions. The XEB circuit fidelity is then given as

$$\mathcal{F}_{\text{XEB}} = \frac{H(p, q) - H(p, u)}{H(p, p) - H(p, u)} \equiv \frac{m_U - u_U}{e_U - u_U}, \qquad (25)$$

where $u(x) = 1/d$ is the uniform probability distribution on the bitstrings. This expression can be understood as the difference in the ideal to measured and ideal to uniform cross entropies, normalized by the difference if the measured distribution was to perfectly match the ideal distribution (i.e. $p(x_i) = q(x_i)$ for all i).

An additional feature of the XEB routine is that at each depth m in the XEB circuits, the so-called speckle purity γ can be used to estimate the decoherence-limited cycle fidelity. It is calculated using the measured bitstring probability distributions as

$$\gamma(m) = \text{Var}(p_m)\frac{d^2(d+1)}{(d-1)}. \qquad (26)$$

Here p_m is the measured probability distribution for bitstrings at depth m in our XEB circuits, where $\text{Var}(p_m) = (d-1)/d^2(d+1)$ for ideal pure states.
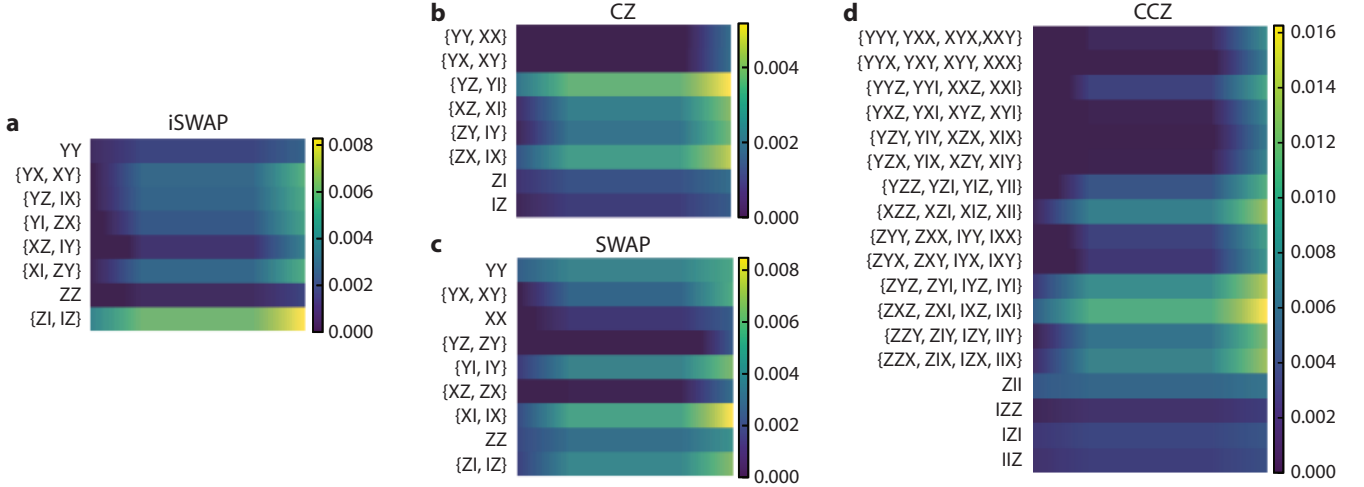
Extended gate verification

Two-qubit gates: The implemented unitaries are also benchmarked using quantum process tomography

(QPT), which can be used to approximate the residual coherent errors. For example, single-qubit Z gates can be approximated using the extracted Pauli transfer matrix (PTM) $\mathcal{R}$ using Nelder-Mead least square optimization. The PTMs for the realized gates are shown in Extended Data Fig. 7**a-c**. They can be reverted using the ideal PTMs to find the error PTMs $\mathcal{R}_{\text{error}} = \mathcal{R}_{\text{exp}}\mathcal{R}_{\text{ideal}}^{-1}$, which is useful in prescribing the residual errors to Pauli channels (Extended Data Fig. 7**d-f**). The process fidelity $\mathcal{F}_{\text{p}}$ and gate fidelity $\mathcal{F}_{\text{g}}$ are extracted following $\mathcal{F}_{\text{p}} = \text{Tr}(\mathcal{R}_{\text{ideal}}^T\mathcal{R}_{\text{exp}})/d^2$ and $\mathcal{F}_{\text{g}} = (d\mathcal{F}_{\text{p}} + 1)/(d + 1)$, where $d = 4$ is the dimension of the two-qubit system. For the displayed iSWAP, CZ, and SWAP PTMs, the extracted gate fidelities are 98.4%, 99.8%, and 98.9%, respectively. Since the extracted PTMs are sensitive to SPAM errors and maximum-likelihood estimation, the fidelities should only be viewed as rough approximation, and their best utilization is for calibration.

CCZ gate: To gauge the stability of the calibration, we continuously monitor the dressed cycle fidelity over 30 consecutive iterations taking over eight hours using CB (Extended Data Fig. 8**a**). Although the sequence consists of multiple gates, we only observe small variation in the fidelity which do not break the limits imposed by coherence time fluctuations. We additionally verify the gate fidelity using cross-entropy benchmarking (XEB), achieving an average XEB fidelity of 93.3(2)% (Extended Data Fig. 8**b,c**), consistent with the CB result. Note that this fidelity includes the error from single-qubit gates used to construct random cycles. XEB also allows us to extract the speckle purity, which is shown to be approximately the same as the cycle fidelity (Extended Data Fig. 8**c**). This implies that the gate is coherence-limited.

Error budgets

To estimate the dephasing-limited fidelity, we first assume that the qubit decays at a rate Γ_1 and dephases at a rate Γ_ϕ, where these rates are related to the relax-

Extended Data Fig. 9. **Error classification**. Pauli noise reconstruction (PNR) results showing the dominant errors impacting **a,** iSWAP, **b,** CZ, **c,** SWAP, and **d,** CCZ gates. The y-axes label the most dominant Pauli Kraus errors for each gate, the cell color denotes the error rate, and the cell gradient defines the 95% confidence interval uncertainty. Pauli errors grouped in curly brackets denote degenerate gate errors which cannot be distinguished due to the effect of the gate itself.

ation time T_1 and decoherence time T_2 as $\Gamma_1 = 1/T_1$, $\Gamma_2 = 1/T_2$. A Pauli transfer matrix (PTM) of a single-qubit decoherence channel for a duration τ is given as

$$\mathcal{E}(\tau) = \begin{pmatrix} 1 & 0 & 0 & 0 \\ 0 & e^{-\Gamma_2\tau} & 0 & 0 \\ 0 & 0 & e^{-\Gamma_2\tau} & 0 \\ 0 & 0 & 0 & e^{-\Gamma_1\tau} \end{pmatrix}. \qquad (27)$$

In the absence of non-Markovian errors such as leakage and crosstalk, the PTM of a Pauli-twirled n-qubit channel is simply given by the tensor product $\mathcal{E}^{\otimes n}$. The process fidelity limited by decoherence can thus be written as
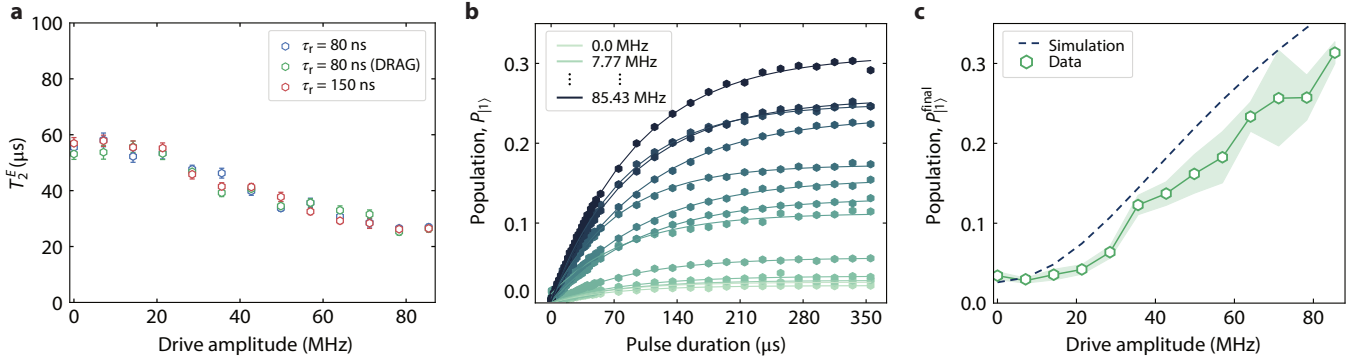
$$\begin{aligned} \mathcal{F}_{\mathrm{p}} &= \frac{1}{4^n}\mathrm{Tr}[\mathcal{E}^{\otimes n}] \\ &= \frac{1}{4^n}\prod_{i=1}^{n}\left(1 + e^{-\Gamma_1^{(i)}\tau} + 2e^{-\Gamma_2^{(i)}\tau}\right), \end{aligned} \qquad (28)$$

where $\Gamma_1^{(i)}$ and $\Gamma_2^{(i)}$ denote the energy relaxation and dephasing rates of qubit i, respectively.

Using Eq. (28), we estimate the coherence-limited fidelities using the best undriven T_1 and T_2^E times for the upper bound, and the worst dynamical values for the lower bound. The lower fidelity bounds for iSWAP, CZ, SWAP, and CCZ gates are {99.2%, 99.4%, 99.1%, 95.1%} and the upper bounds are {99.6%, 99.7%, 99.5%, 97.1%}. Although this approach only gives approximate limits, they are already remarkably close to the obtained fidelities. We note that the CCZ sequence contains four different pulses involving different qubit pairs, so it is difficult to choose the appropriate coherence times for the analysis. However, the speckle purity measurement (Extended Fig. 8c) reveals that it should be dephasing-limited.

In practice, the ramp times ($\sim$50-100 ns) constitute a majority of the pulses used for the gates ($\sim$200 ns), as opposed to the long pulses with mostly fixed amplitudes used in the dynamical coherence measurements (Fig. 3b). Besides, different gates require different combinations of pulse amplitudes and ramp times, making it challenging to systematically select the right coherence values for our approximation. Therefore, we believe that it is reasonable to estimate the fidelity limits using the presented approach. A more rigorous estimation may ideally involve a numerical Floquet simulation with the integration of a time-dependent mapping. Future research to elucidate such dynamics, shedding light on the dephasing process, will help establish the required techniques to study spurious effects associated with Floquet-engineered interactions.

To reconstruct the dominant error channels impacting the iSWAP, CZ, SWAP, and CCZ gates, we utilize Pauli noise reconstruction (PNR)[51], also referred to as cycle error reconstruction[52]. PNR reconstructs the Pauli Kraus errors affecting each gate from a set of CB measurements (see the Supplemental Material of Ref.[52] for a detailed discussion). For example, in Extended Data Fig. 9, we observe that the dominant error channel for the iSWAP gate is a Z error on either qubit, even though ZZ appears to be largely suppressed (note that IZ and ZI cannot be distinguished, due to the fact that the iSWAP gate transforms one into the other). For the CZ gate, we observe that Y-type errors on Q_1 or X-type errors on Q_2 are the most dominant. The SWAP gate is mostly affected by X- or Z-type errors on either qubit. While the error generators for the CCZ are more difficult to interpret, we consistently observe that Z-type errors on Q_1, X- or Y-type errors on Q_2, and Z-type errors on Q_3 are the most dominant.

Extended Data Fig. 10. **Dressed decoherence**. **a,** Dependence of Q_1's echo time T_2^E on the drive amplitude and pulse shape. **b,** Q_1's excited state population after the mapping using a pulse with parametrized amplitude and duration. The qubit is first initialized in $|0\rangle$. **c,** Comparison between obtained excited state populations after a 355-μs-long pulse at various driving amplitudes (green markers) and numerically simulated values (blue dashed line).

Dressed heating and dephasing

We utilize the single-shot readout capability of the measurement setup (cf. Extended Data Fig. 2**a**) to selectively measure the dynamics of Q_1 under the drive. To measure the relaxation process, the qubit is first prepared in state $|1\rangle$ by applying a π pulse to a pre-selected $|0\rangle$ state. Then, a microwave pulse with variable amplitude and duration is applied to the qubit. The ramp time is chosen to be 100 ns to ensure adiabaticity for the amplitude values shown. We discard the data in which small oscillation appears, which correspond to the non-adiabatic regime. The qubit is measured dispersively after the off-resonant pulse, and then post-selected in the $|0\rangle$ state. The excitation dynamics is measured in a similar fashion, with the qubit prepared in the ground state and post-selected in the $|1\rangle$ state. For T_2^E, a π pulse on the undriven qubit is inserted between two Floquet drive pulses with the same ramp and duration times. This refocusing pulse is orthogonal in phase to the $\pi/2$ projection pulses. To ensure the passive reset of the qubit, a delay time of 50 μs is added between neighboring sequences.

To verify that the reduction in the obtained T_2^E times is not due to nonadiabatic effects, we repeat the measurements with different ramp times τ_r and DRAG co-efficients λ_{DRAG}, and still observe a consistent decrease with respect to the pulse amplitude, as shown in Extended Data Fig. 10**a**. Intriguingly, we also find a consistent heating effect that increases the excited state population after the mapping, suggesting a change in the effective qubit temperature. Notably, although the population of the qubit increases monotonically with respect to the drive amplitude (Extended Data Fig. 10**b**), the extracted relaxation and excitation rates do not show any obvious trend (Fig. 3**b**).

We simulate this effect numerically by projecting the decoherence mechanisms onto the Floquet basis. Using the experimentally obtained ratio $\nu = P_{|1\rangle}^{\mathrm{final}}/P_{|0\rangle}^{\mathrm{final}} = 0.027$ of the undriven qubit in equilibrium (355 μs after initialization), we assume a finite relaxation rate $\Gamma_\downarrow = (T_1)^{-1}/(1 + \nu)$, excitation rate $\Gamma_\uparrow = (T_1)^{-1} - \Gamma_\downarrow$, and pure dephasing rate $\Gamma_\phi = (T_2^E)^{-1} - (2T_1)^{-1}$, where T_1 and T_2^E are taken from Table II. Next, we simply map the jump operators $\hat{L}_- = \sqrt{\Gamma_\downarrow}|0\rangle\langle 1|$, $\hat{L}_+ = \sqrt{\Gamma_\downarrow}|1\rangle\langle 0|$, and $\hat{L}_\phi = \sqrt{\Gamma_\phi/2}\hat{\sigma}_z$ onto the Floquet basis, then evolve the system starting from the ground state using the Lindblad master equation. The result shown in Extended Data Fig. 10**c** agrees well with the experimentally obtained data (previously shown in the inset of Fig. 3**b**).